Typeset using LaTeX **twocolumn** style in AASTeX631

Draft version May 5, 2022

CO Line Emission Surfaces and Vertical Structure in Mid-Inclination Protoplanetary Disks

Charles J. Law [1], Sage Crystian [1], Richard Teague [1], Karin I. Öberg [1], Evan A. Rich [2], Sean M. Andrews [1], Jaehan Bae [3], Kevin Flaherty [4], Viviana V. Guzmán [5], Jane Huang [2,*], John D. Ilee [6], Joel H. Kastner [7], Ryan A. Loomis [8], Feng Long [1], Laura M. Pérez [9,10], Sebastián Pérez [11,12], Chunhua Qi [1], Giovanni P. Rosotti [13], Dary Ruíz-Rodríguez [8], Takashi Tsukagoshi [14] and David J. Wilner [1]

[1] *Center for Astrophysics | Harvard & Smithsonian, 60 Garden St., Cambridge, MA 02138, USA*
[2] *Department of Astronomy, University of Michigan, 323 West Hall, 1085 South University Avenue, Ann Arbor, MI 48109, USA*
[3] *Department of Astronomy, University of Florida, Gainesville, FL 32611, USA*
[4] *Department of Astronomy and Department of Physics, Williams College, Williamstown, MA 01267, USA*
[5] *Instituto de Astrofísica, Pontificia Universidad Católica de Chile, Av. Vicuña Mackenna 4860, 7820436 Macul, Santiago, Chile*
[6] *School of Physics and Astronomy, University of Leeds, Leeds, UK, LS2 9JT*
[7] *Chester F. Carlson Center for Imaging Science, School of Physics & Astronomy, and Laboratory for Multiwavelength Astrophysics, Rochester Institute of Technology, Rochester, NY 14623, USA*
[8] *National Radio Astronomy Observatory, 520 Edgemont Rd., Charlottesville, VA 22903, USA*
[9] *Departamento de Astronomía, Universidad de Chile, Camino El Observatorio 1515, Las Condes, Santiago, Chile*
[10] *Núcleo Milenio de Formación Planetaria (NPF), Chile*
[11] *Center for Interdisciplinary Research in Astrophysics and Space Exploration (CIRAS), Universidad de Santiago de Chile*
[12] *Departamento de Física, Universidad de Santiago de Chile. Avenida Ecuador 3493, Estación Central, Santiago, Chile*
[13] *Leiden Observatory, Leiden University, P.O. Box 9513, NL-2300 RA Leiden, the Netherlands*
[14] *National Astronomical Observatory of Japan, 2-21-1 Osawa, Mitaka, Tokyo 181-8588, Japan*

ABSTRACT

High-spatial-resolution CO observations of mid-inclination (≈30-75°) protoplanetary disks offer an opportunity to study the vertical distribution of CO emission and temperature. The asymmetry of line emission relative to the disk major axis allows for a direct mapping of the emission height above the midplane, and for optically-thick, spatially-resolved emission in LTE, the intensity is a measure of the local gas temperature. Our analysis of ALMA archival data yields CO emission surfaces, dynamically-constrained stellar host masses, and disk atmosphere gas temperatures for the disks around: HD 142666, MY Lup, V4046 Sgr, HD 100546, GW Lup, WaOph 6, DoAr 25, Sz 91, CI Tau, and DM Tau. These sources span a wide range in stellar masses (0.50-2.10 $M_\odot$), ages (∼0.3-23 Myr), and CO gas radial emission extents (≈200-1000 au). This sample nearly triples the number of disks with mapped emission surfaces and confirms the wide diversity in line emitting heights ($z/r \approx 0.1$ to $\gtrsim 0.5$) hinted at in previous studies. We compute radial and vertical CO gas temperature distributions for each disk. A few disks show local temperature dips or enhancements, some of which correspond to dust substructures or the proposed locations of embedded planets. Several emission surfaces also show vertical substructures, which all align with rings and gaps in the millimeter dust. Combining our sample with literature sources, we find that CO line emitting heights weakly decline with stellar mass and gas temperature, which, despite large scatter, is consistent with simple scaling relations. We also observe a correlation between CO emission height and disk size, which is due to the flared structure of disks. Overall, CO emission surfaces trace ≈2-5× gas pressure scale heights (H_g) and could potentially be calibrated as empirical tracers of H_g.

Keywords: Protoplanetary disks (1300) — Planet formation (1241) — CO line emission (262) — High angular resolution (2167)

1. INTRODUCTION

Protoplanetary disks exhibit flared emitting surfaces set by hydrostatic equilibrium, as first recognized in the spectral energy distributions of their host stellar systems (Kenyon & Hartmann 1987). Disks are also highly stratified in their physical and chemical properties (Williams & Cieza 2011) with vertical distributions of molecular material that are greatly influenced by gradients in physical conditions such as gas temperature, density, or radiation (e.g., Walsh et al. 2010; Fogel et al. 2011), the efficiency of turbulent vertical mixing (e.g., Ilgner et al. 2004; Semenov & Wiebe 2011; Flaherty et al. 2020), or the presence of meridional flows driven by embedded planets (e.g., Morbidelli et al. 2014; Teague et al. 2019; Yu et al. 2021).

A detailed understanding of this complex vertical structure is required to interpret kinematic signals in CO emission (Perez et al. 2015; Pérez et al. 2018; Pinte et al. 2019; Disk Dynamics Collaboration et al. 2020; Pérez et al. 2020; Teague et al. 2021) and the effects of embedded protoplanets on the density distribution, temperature, and pressure of gas in disks (Teague et al. 2018; Calcino et al. 2022; Izquierdo et al. 2022). Accurate dynamical mass estimates derived from line emission rotation maps also require well-constrained line emitting heights (Casassus & Pérez 2019; Veronesi et al. 2021). This is especially critical as most line emission does not originate from the midplane but from layers higher up in the disk (Dartois et al. 2003; Piétu et al. 2007). As a result, line emission surfaces also trace the vertical temperature structure of disks (Dartois et al. 2003; Rosenfeld et al. 2013; Pinte et al. 2018; Teague et al. 2020; Law et al. 2021a; Flores et al. 2021), provide important inputs to disk thermochemical models (Zhang et al. 2021; Calahan et al. 2021; Schwarz et al. 2021), and serve as useful diagnostics to disentangle observational signatures of planet-disk interactions versus depletions in gas surface density (Dong et al. 2019; Rab et al. 2020; Bae et al. 2021; Alarcón et al. 2021). Emission surfaces are also relevant for the chemistry of planet formation, as they are required to assess how well connected molecular gas abundances derived from line observations are to their abundances in planet-forming disk midplanes.

There are several approaches to obtaining information about the vertical distribution of gas in disks. Vertical structures have been observed in highly-inclined or edge-on disks, which allow a direct mapping of emission distributions (e.g., Guilloteau et al. 2016; Dutrey et al. 2017; Teague et al. 2020; Podio et al. 2020; Ruíz-Rodríguez et al. 2021; Flores et al. 2021; Villenave et al. 2022). However, with sufficient angular resolution and surface brightness sensitivity it is possible to extract disk vertical structures from mid-inclination (≈30–75°) disks by exploiting spatially-resolved emission from elevated regions above and below the midplane (e.g., de Gregorio-Monsalvo et al. 2013; Rosenfeld et al. 2013; Isella et al. 2018). In these cases, the emission heights of bright molecular lines can be directly determined (Pinte et al. 2018; Rich et al. 2021; Paneque-Carreño et al. 2021; Law et al. 2021a). This approach expands the sample of disks whose vertical structure can be mapped and allows us to relate vertical gas structure to that of the radial continuum, which is often inaccessible in edge-on disks due to high optical depths.

With a known temperature structure, it is also possible to estimate indirect line emission heights based on inferred brightness temperatures for disks with low inclinations (e.g., Teague & Loomis 2020; Öberg et al. 2021a), or for molecules with weaker emission where direct mapping is not feasible (e.g., Ilee et al. 2021). Without such a temperature structure, relative stratification patterns between different molecular emission lines can be discerned by modeling multiple line fluxes (e.g., Bruderer et al. 2012; Fedele et al. 2016).

As part of the Molecules with ALMA at Planet-forming Scales (MAPS) (Öberg et al. 2021b) ALMA Large Program, Law et al. (2021a) directly mapped the emission surfaces of several CO isotopologues in the disks around IM Lup, GM Aur, AS 209, HD 163296, and MWC 480. The authors found a wide range in CO line emitting heights and identified tentative trends suggesting that disks with lower host star masses and larger CO gas disks had more vertically extended emission surfaces. However, firm conclusions were precluded by the small sample size of five disks.

Here, we extract CO emission surfaces for ten disks with favorable orientations with respect to our line-of-sight that have been previously observed at sufficiently high spatial resolution and sensitivity. We describe the ALMA archival data from which we draw our disk sample and briefly detail our surface extraction methods in Section 2. In Section 3, we present the derived emission surfaces, compare them with previous millimeter and NIR observations, and calculate radial and vertical temperature profiles. We explore possible origins of the observed disk vertical structures and examine the relationship between line emission surfaces and gas pressure scale heights in Section 4. We summarize our conclusions in Section 5.

* NASA Hubble Fellowship Program Sagan Fellow

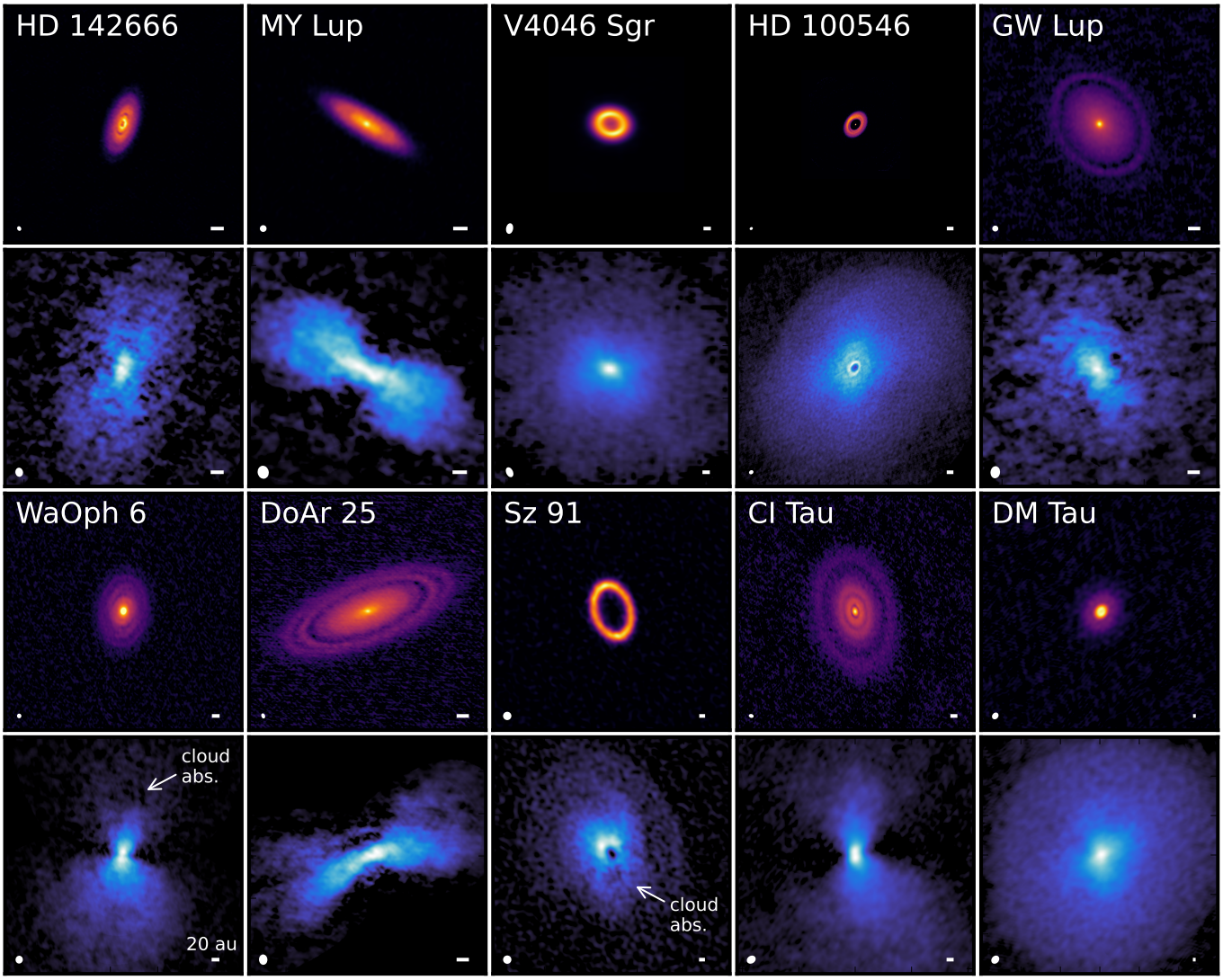

Figure 1. Millimeter continuum images (first and third rows) and CO zeroth moment maps (second and fourth rows) for all disks. Line emission is from CO J=2–1 and the continuum is at 1.3 mm, except for V4046 Sgr and Sz 91, which show the 870 μm continuum; and for V4046 Sgr, Sz 91, and CI Tau, which show CO J=3–2 line emission. Panels for each disk have the same field of view. Color stretches were individually optimized and applied to each panel to increase the visibility of outer disk structure. The asymmetries present in WaOph 6 and Sz 91 are due to cloud contamination and are labeled in the maps of each disk. The dark lane seen in DoAr 25 traces the disk midplane and is visible due to the relatively high inclination of this source. The synthesized beam and a scale bar indicating 20 au is shown in the lower left and right corner, respectively, of each panel. Details about each of the observations are found in Section 2.1 and Table 1.

2. OBSERVATIONS AND ANALYSIS

2.1. *Archival Data*

We searched the ALMA archive for CO line observations of protoplanetary disks with inclinations of 30-75°and sufficiently high angular resolutions, line sensitivities, and velocity resolutions to derive emission surfaces.

We made use of the publicly available, science ready CO J=2–1 image cubes from the ALMA Large Program DSHARP[1] (Andrews et al. 2018). We selected those disks with favorable inclinations for surface extractions and excluded those disks with prohibitively severe cloud contamination. After these considerations, we were left with the following sources: HD 142666, MY Lup, GW Lup, WaOph 6, and DoAr 25. We also excluded the disks observed as part of MAPS, as they already have well-constrained emission surfaces (Law et al. 2021a). In addition, we used ALMA observations of the disks around: V4046 Sgr (Ruíz-Rodríguez et al. 2019), HD 100546 (Pérez et al. 2020), Sz 91 (Tsukagoshi et al. 2019), CI Tau (Rosotti et al. 2021), and DM Tau (Flaherty et al. 2020). All data were obtained from the original authors and observational details may be found in the corresponding references. The data for V4046 Sgr, Sz 91, and CI Tau are CO J=3–2, while DM Tau and HD 100546 are CO J=2–1. Velocity resolutions spanned from 0.16-0.5 km s^{-1}, while typical angular resolutions were ≈0.″07–0.″14, or 10-20 au, with the exception of DM Tau (0.″36; 52 au). The large size of the DM Tau CO gas disk and its highly flared nature (e.g., Flaherty et al. 2020) made surface extraction possible even with a coarser angular resolution.

Overall, the sources in our sample span a wide range in both stellar properties, such as masses (0.50-2.10 $M_\odot$), spectral types (M-B), bolometric luminosities (0.24-23.4 $L_\odot$), and ages (∼0.3-23 Myr), as well as disk physical characteristics, such as CO gas disk radial emission extents (≈200-1000 au), and includes both full and transition disks. Several of our sources exhibit mild-to-moderate cloud contamination, in which the ambient cloud significantly absorbs disk line emission with overlapping velocities. This is identified through visual inspection of channel maps and manifests as spatial brightness asymmetries in images of the CO line emission. Table 1 shows a summary of source characteristics, including the ALMA Project Codes for the corresponding archival data.

Figure 1 shows an overview of the disk sample in millimeter continuum emission and CO velocity-integrated intensity, or "zeroth moment," maps. All continuum images are taken from previously published ALMA observations. Specifically, we show 1.3 mm continuum images of HD 142666, MY Lup, GW Lup, WaOph 6, and DoAr 25 (Andrews et al. 2018); HD 100546 (Pérez et al. 2020); CI Tau (Clarke et al. 2018), and DM Tau (Flaherty et al. 2020). We show 870 μm continuum images of V4046 Sgr (Ruíz-Rodríguez et al. 2019) and Sz 91 (Canovas et al. 2016). We generated the zeroth moment maps from the CO image cubes using `bettermoments` (Teague & Foreman-Mackey 2018) with no sigma clipping and Keplerian masks based on the parameters in Table 1. See Appendix A for more details on the moment map generation process.

For the calculation of gas temperatures with the full Planck function, we also made use of the line+continuum image cubes. These were also obtained from the original authors, with the exception of the DSHARP sources, where we manually re-imaged the line emission cubes with the continuum following the same imaging procedures used to produce the original CO cubes (Andrews et al. 2018). We also re-imaged archival data (PI: G. van der Plas, 2015.1.00192.S) of the HD 97048 disk to derive a line+continuum image cube (Appendix C). This source is not formally part of our sample as it already has a directly-mapped CO line emission surface from Rich et al. (2021) but lacks an estimate of its CO gas temperature structure. While the CO thermal structure of the HD 97048 disk is of interest in its own right, it is also required for establishing a homogeneous sample for source-to-source comparisons.

The line-only and line+continuum image cubes as well as all zeroth moment maps are publicly available on Zenodo doi: 10.5281/zenodo.6410045.

2.2. *Methods*

2.2.1. *Surface Extraction*

We used the line emission image cubes to extract vertical emission surfaces for each disk, closely following the methods of Law et al. (2021a). In short, we leveraged the spatially-resolved emission asymmetry visible in the channel maps (see Figure 15, Appendix B) to constrain the vertical emission height. To do so, we used the `disksurf` (Teague et al. 2021) python code, which implements this method as well as several filtering steps to extract more accurate emission surfaces.

For each image cube, we restricted the position-position-velocity regions from which we extracted surfaces to those contained in disk-specific Keplerian masks based on CO emission morphology and source characteristics. We then manually excluded those channels where the front and back disk sides could not be dis-

[1] https://bulk.cv.nrao.edu/almadata/lp/DSHARP/

Table 1. Stellar and Disk Characteristics

Source	Spectral Type	Distance[a] (pc)	incl. (°)	PA (°)	M_*[b] ($M_\odot$)	L_* ($L_\odot$)	Age[c] (Myr)	v_{sys}[b] (km s^{-1})	cloud contam.	ALMA Project Code	Ref.
HD 142666	A8	145	62.2	162.1	1.73	9.1	13	4.37	...	2016.1.00484.L	1,2
MY Lup	K0	157	73.2	58.8	1.27	0.87	10	4.71	mild	2016.1.00484.L	1,2
V4046 Sgr[d]	K5,K7	71	34.7	75.7	1.72	0.86	23	2.93	...	2016.1.00315.S	3-8
HD 100546	B9	108	41.7	146.0	2.10	23.4	5	5.65	...	2016.1.00344.S	9-13
GW Lup	M1.5	154	38.7	37.6	0.62	0.33	2	3.69	...	2016.1.00484.L	1,2
WaOph 6	K6	122	47.3	174.2	1.12	2.9	0.3	4.21	mild	2016.1.00484.L	1,2
DoAr 25	K5	138	67.4	110.6	1.06	0.95	2	3.38	moderate	2016.1.00484.L	1,2
Sz 91	M0	158	49.7	18.1	0.55	0.26	3-7	3.42	moderate	2012.1.00761.S	14-16
CI Tau	K5.5	160	49.2	11.3	1.02	1.26	2	5.70	moderate	2017.A.00014.S	17-20
DM Tau	M1	143	36.0	154.8	0.50	0.24	1-5	6.04	...	2016.1.00724.S	4,21-22
HD 97048	A0V	184	41.0	3.0	2.70	44.2	4	4.55	moderate	2015.1.00192.S	23-25

[a] All distances are from *Gaia* DR3 (Gaia Collaboration et al. 2021; Bailer-Jones et al. 2021).

[b] Dynamical masses and systemic velocities are derived in this work (see Section 3.6).

[c] Stellar ages are likely uncertain by at least a factor of two.

[d] V4046 Sgr hosts a protoplanetary disk orbiting a binary star system. The individual stellar spectral types are listed, along with the total stellar mass and luminosity.

NOTE—References are: 1. Andrews et al. (2018); 2. Huang et al. (2018); 3. Quast et al. (2000); 4. Flaherty et al. (2020); 5. Rosenfeld et al. (2012); 6. Mamajek & Bell (2014); 7. Torres et al. (2006); 8. Binks & Jeffries (2014); 9. Pineda et al. (2014); 10. Pineda et al. (2019); 11. Vioque et al. (2018); 12. Fedele et al. (2021); 13. Casassus & Pérez (2019); 14. Romero et al. (2012); 15. Tsukagoshi et al. (2019); 16. Maucó et al. (2020); 17. Clarke et al. (2018); 18. Simon et al. (2017); 19. Donati et al. (2020); 20. Simon et al. (2019); 21. Guilloteau et al. (2014); 22. van den Ancker et al. (1998); 23. Walsh et al. (2016); 24. van der Plas et al. (2017); 25. Asensio-Torres et al. (2021).

entangled as well as those channels with severe cloud contamination. After the initial extraction, we filtered pixels based on priors of disk physical structure. We removed those pixels with extremely high z/r values (upper boundaries ranging from 0.45 to 1.0 depending on the disk) and large negative z values, as the emission must arise from at least the midplane. We allowed points with small negative values, i.e., $z/r > -0.1$, to remain to avoid positively biasing our averages to non-zero z values. To minimize contamination from background thermal noise, which can confuse the identification of emission peaks, we also filtered points based on surface brightness thresholds, which varied from 1×rms (HD 142666) to 8×rms (DM Tau). The wide range in thresholds was a result of our heterogeneous sample with differing line sensitivities, which was driven in part by varied beam sizes. For instance, the beam size of the DM Tau observations is approximately five times greater than that of the HD 142666 image cubes. This is comparable to the source size ratio between the two disks, i.e., the DM Tau disk is nearly five times larger than that of HD 142666. In general, we prioritized the extraction of the maximum number of reliable emission surface pixels and visually confirmed the quality of each extraction before and after the filtering process. For further details about this procedure, see Law et al. (2021a).

Emission surfaces were extracted on a per-pixel basis. We first must assume an inclination and position angle of each disk (Table 1). Then, for each pixel associated with the emitting surface, we obtained a deprojected radius r, emission height z, surface brightness I_ν, and channel velocity v. To further reduce scatter in these surfaces, we used two different binning methods: (1) we radially binned the surfaces using bins equal to one-half of the FWHM of the beam major axis; (2) and calculated a moving average with a minimum window size of 1/2× the beam major axis FWHM. The binned surfaces resulted in a uniform radial sampling, while the moving averages retained a finer radial sampling, which is essential for identifying subtle vertical perturbations in the emission surfaces that may be, e.g., associated with features in the dust continuum or putative planet locations. These are the same binning methods employed in Law et al. (2021a), but with twice as large a radial bin

Table 2. Parameters for CO Emission Surface Fits

Source	Line	Exponentially-Tapered Power Law				
		$r_{\rm fit,\,max}$ [']	z_0 [']	ϕ	$r_{\rm taper}$ [']	ψ
HD 142666	J=2−1	0.80	$0.09^{+0.12}_{-0.03}$	$0.50^{+0.44}_{-0.27}$	$1.13^{+0.59}_{-0.48}$	$2.37^{+5.10}_{-1.79}$
MY Lup	J=2−1	1.00	$0.21^{+0.14}_{-0.08}$	$1.28^{+0.40}_{-0.41}$	$0.80^{+0.08}_{-0.10}$	$3.95^{+2.10}_{-1.29}$
V4046 Sgr	J=3−2	2.25	$0.28^{+0.08}_{-0.03}$	$0.59^{+0.23}_{-0.16}$	$1.99^{+0.18}_{-0.34}$	$2.59^{+1.22}_{-0.92}$
HD 100546	J=2−1	1.20	$0.35^{+0.21}_{-0.07}$	$1.09^{+0.29}_{-0.18}$	$1.02^{+0.08}_{-0.20}$	$2.57^{+0.95}_{-0.79}$
GW Lup	J=2−1	1.20	$0.22^{+0.07}_{-0.02}$	$0.76^{+0.19}_{-0.14}$	$1.22^{+0.21}_{-0.11}$	$5.91^{+2.48}_{-3.71}$
WaOph 6	J=2−1	1.40	$0.37^{+0.24}_{-0.10}$	$1.77^{+0.36}_{-0.30}$	$1.13^{+0.15}_{-0.25}$	$2.52^{+1.27}_{-0.78}$
DoAr 25	J=2−1	1.95	$0.31^{+0.02}_{-0.01}$	$1.54^{+0.13}_{-0.12}$	$1.61^{+0.03}_{-0.04}$	$5.85^{+1.05}_{-0.86}$
Sz 91[a]	J=3−2	1.60	$0.91^{+0.07}_{-0.12}$	$2.59^{+0.12}_{-0.15}$	$0.86^{+0.06}_{-0.03}$	$1.99^{+0.18}_{-0.16}$
CI Tau	J=3−2	1.40	$0.32^{+0.07}_{-0.03}$	$1.48^{+0.16}_{-0.14}$	$2.07^{+0.58}_{-0.31}$	$2.61^{+0.97}_{-1.06}$
DM Tau	J=2−1	3.00	$0.82^{+0.06}_{-0.05}$	$1.85^{+0.08}_{-0.07}$	$1.79^{+0.11}_{-0.12}$	$1.67^{+0.10}_{-0.10}$
HD 97048[b]	*J=2−1*	*2.65*	$0.31^{+0.02}_{-0.01}$	$1.16^{+0.09}_{-0.07}$	$2.74^{+0.09}_{-0.13}$	$2.81^{+0.54}_{-0.50}$

[a] Fit only considering the inner 1.″60 to avoid elevated, diffuse material at larger radii, which is not well-fit by an exponentially-tapered power law.

[b] CO line emission surface rederived and fit with an exponentially-tapered power law for consistency. See Appendix C and Rich et al. (2021).

and window size, due to the generally less sensitive data used here relative to that of the MAPS sample (Öberg et al. 2021b).

All three types of line emission surfaces – individual measurements, radially-binned, and moving averages – are made publicly available. Throughout this work, we sometimes radially bin these data products further for visual clarity, but all quantitative analysis is done using the original binning of each type of emission surface.

2.2.2. *Analytical Fitting*

To more readily compare with other observations and to facilitate their incorporation into models, we fitted exponentially-tapered power laws to all CO emission surfaces. This fit describes both the flared surfaces in the inner disk and the plateau/turnover region in the outer disk. We adopt the same functional form as in Law et al. (2021a):

$$z(r) = z_0 \times \left(\frac{r}{1''}\right)^{\phi} \times \exp\left(-\left[\frac{r}{r_{\rm taper}}\right]^{\psi}\right) \qquad (1)$$

where z_0, ϕ, and ψ are non-negative. A value of $\phi > 1$ indicates that z/r increases with radius, while $0 < \phi < 1$ tends toward a flat $z(r)$ profile.

All fits were performed using the Monte Carlo Markov Chain (MCMC) sampler implemented in `emcee` (Foreman-Mackey et al. 2013) to estimate the posterior distributions of the following parameters: z_0, ϕ, $r_{\rm taper}$, and ψ. The radial range of each fit is given by $r_{\rm fit,\,max}$ in Table 2. We used 64 walkers which take 1000 steps to burn in and an additional 500 steps to sample the posterior distribution function. We chose an MCMC fitting approach rather than a simple χ^2 minimization, as we found that it better handled the degeneracies between fitted parameters, especially, e.g., between ψ and $r_{\rm taper}$. Table 2 shows all fitted parameters. Isovelocity contours generated using the surface fits from Table 2 are shown in Figure 15 in Appendix B.

3. RESULTS

3.1. *Overview of Emission Surfaces*

Figure 2 shows the CO emission surfaces derived in all disks in our sample. There is considerable disk-to-disk variation in line emitting heights and surface flaring, i.e., how quickly z increases as a function of r. Peak emitting heights range from ≈10-150 au, while typical z/r values span ≈0.1 to $\gtrsim$0.5. HD 142666 hosts the flattest disk, while the DM Tau disk has by far the most elevated emission surface.

Many of the disks exhibit a quick, power-law-like rise in height with radius, which is then followed by a gradual flattening and eventual turnover of their emission surfaces at large radii as, presumably, gas surface densities decrease. However, we sometimes only see either the initial flattening, like in the HD 142666 disk, or the beginning of the turnover phase, such as for the WaOph 6 and DM Tau disks. We suspect that the missing turnovers are simply due to low SNR in the outer regions of some

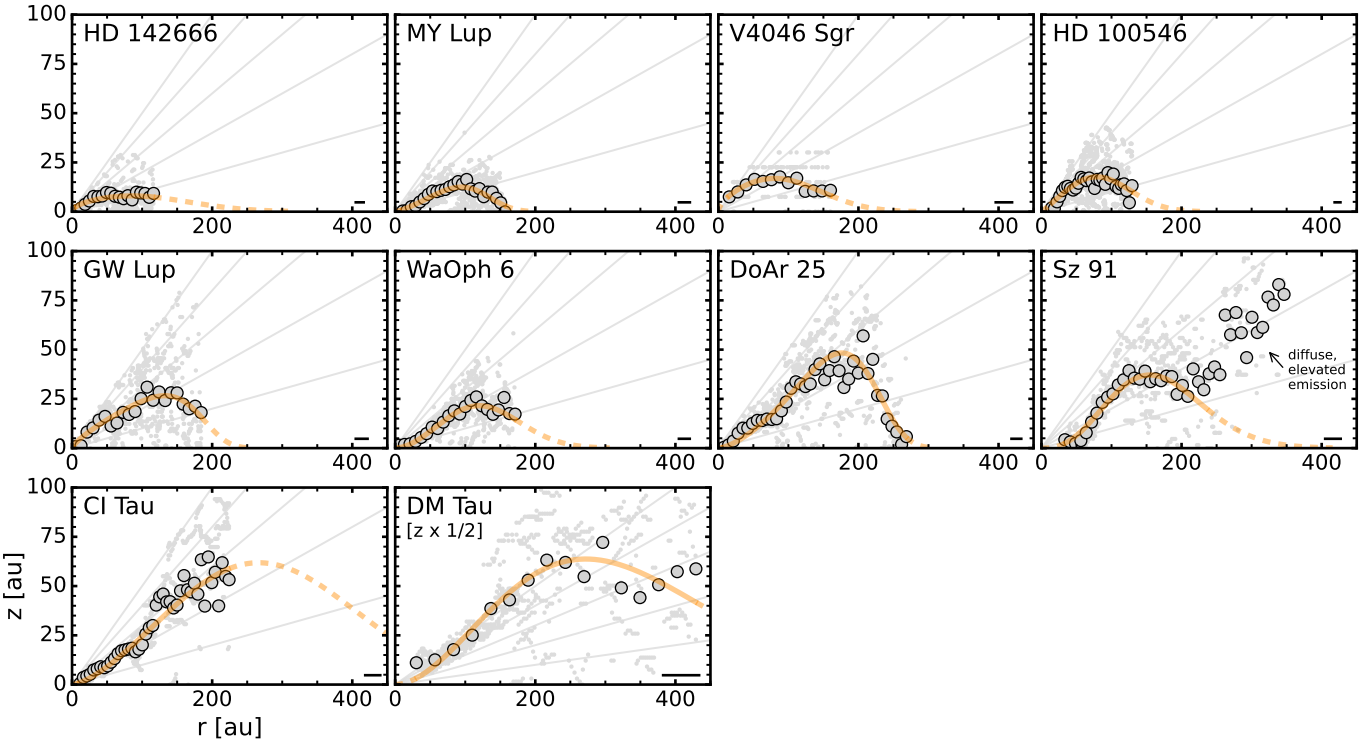

Figure 2. CO emission surfaces for all disks. Large gray points show radially-binned surfaces and small, light gray points represent individual measurements. The orange lines show the exponentially-tapered power law fits from Table 2. The solid lines show the radial range used in the fitting, while the dashed lines are extrapolations. Diffuse, elevated emission present at large radii in the Sz 91 disk is labeled and excluded in the fits. Lines of constant z/r from 0.1 to 0.5 are shown in gray. All panels show a consistent radial and vertical range, except for DM Tau where the vertical extent has been scaled by $\times 1/2$. The FWHM of the major axis of the synthesized beam is shown in the bottom right corner of each panel. The emission surfaces shown in this figure are available as Data behind the Figure.

disks. For sources (e.g., CI Tau) where the turnover is not visible, the r_{taper} and ψ parameters of the analytical fits in Table 2 are highly uncertain.

Notably, the Sz 91 emission surface does not follow this characteristic structure. While we see the flared and plateau phases out to 200 au, emission heights again begin to quickly rise beyond this and do not show any sign of flattening out to ≈350 au. The presence of diffuse emission at large radii in this disk was previously noted by Tsukagoshi et al. (2019), and the derived surface is quite similar to that of CO J=2–1 in the IM Lup disk (Law et al. 2021a). When fitting this disk, we thus restrict our analytic fits to within ≈200 au.

Overall, there is no single characteristic height that all disks share, but instead line emission heights vary by over an order of magnitude, while typical z/r values span at least a factor of five. These results confirm that the diversity previously observed in line emission heights (Law et al. 2021a) is commonplace. To better illustrate this and highlight the geometry of the emission surfaces, Figure 3 shows a 3D representation of the fitted surfaces in our disk sample and from literature sources with directly-mapped CO emission surfaces.

3.2. *Vertical Substructures and Comparison with Millimeter Continuum Features and Kinematic Planetary Signatures*

A few of the emission surfaces in our sample exhibit vertical substructures in the form of dips or prominent changes in emission slope. In Figure 4, a dip at 45 au is evident in the line emitting heights of the HD 100546 disk, while slope changes are seen around 80 au and 90 au in the emission surfaces of the DoAr 25 and CI Tau disks, respectively. A shallow dip is also seen at 50 au in the emission surface of the CI Tau disk.

Each of these vertical substructures radially aligns with dust features. In Figure 4, we overlay the midpoint radial locations of millimeter rings and gaps in all disks. The radial locations of dust substructures indicated for the HD 100546 disk are approximate, since the location of dust features differs by a few 10s of au along different projections due to the azimuthally asymmetric dust emission in this source (Pineda et al. 2019; Pérez et al. 2020; Fedele et al. 2021). The dip in the emission

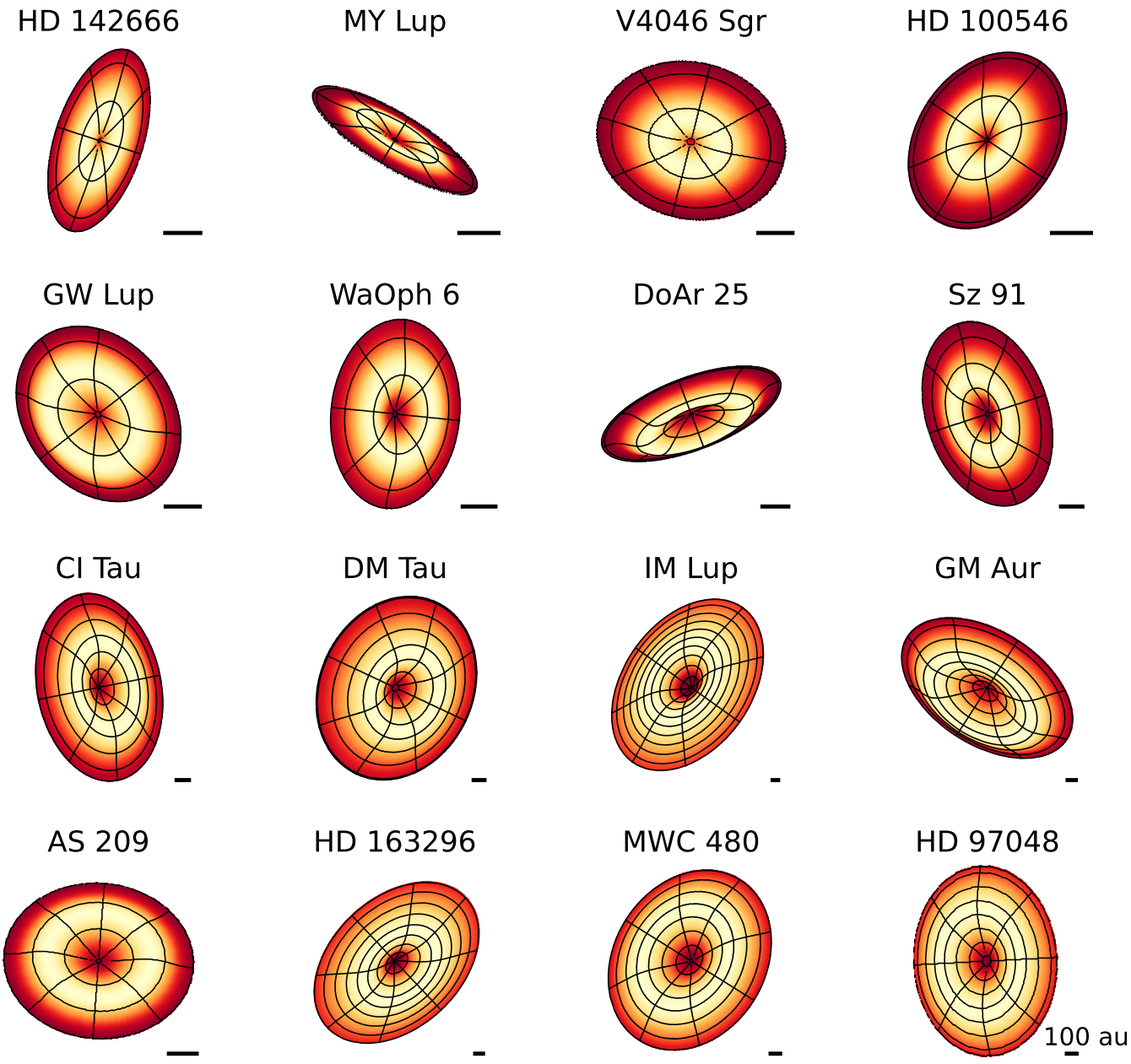

Figure 3. Three-dimensional representations of CO emission surfaces for the disks derived in this work and for the disks around IM Lup, GM Aur, AS 209, HD 163296, and MWC 480 (Law et al. 2021a) and HD 97048 (Rich et al. 2021). Colormaps show the vertical height of each emission surface using exponentially-tapered power law profiles. For each disk, the colormap is normalized to the maximum height and each contour represents a radial distance of 100 au. Surfaces are radially extrapolated beyond the direct surface measurements in Figure 2 to better illustrate their shapes; however, we caution that this sometimes results in a surface that is larger than the total CO gas disk extent. The elevated, diffuse emission at large radii in the Sz 91 and IM Lup disks are not shown. A scale bar indicating 100 au is shown in the lower right corner.

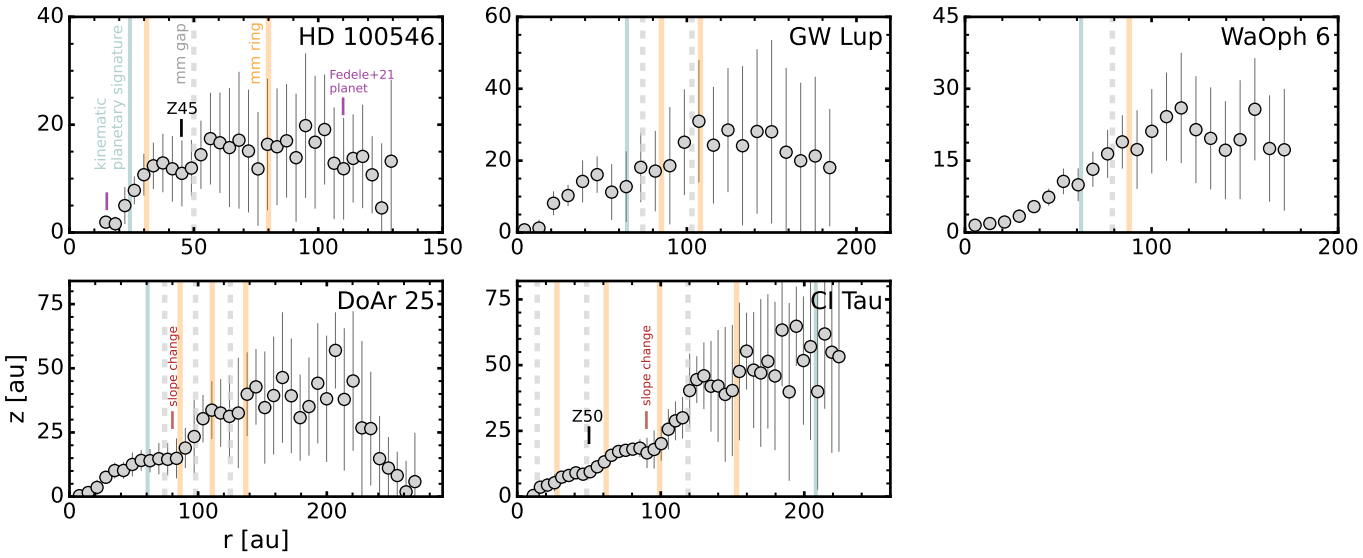

Figure 4. CO emission surfaces for disks with vertical substructures or kinematic planetary signatures. Large gray points show radially-binned surfaces and vertical lines show the 1σ uncertainties in z. Vertical substructures in CO emission surfaces are labeled by their approximate radial location in au following the nomenclature of Law et al. (2021a) and are marked in black, while slope changes are shown in red. The midpoint radial locations of millimeter dust rings and gaps are shown as solid orange and dashed gray lines, respectively, and are compiled from Huang et al. (2018); Clarke et al. (2018); Long et al. (2018); Fedele et al. (2021). Radial locations of dust features in the HD 100546 disk are approximate, due to the azimuthally asymmetric dust emission in this source (Pineda et al. 2019; Pérez et al. 2020; Fedele et al. 2021). The mm gap at 40 au in the HD 100546 disk marks the inner edge of a wide (∼40-150 au) continuum gap. KPSs are marked by blue lines and are from Casassus & Pérez (2019); Pérez et al. (2020); Pinte et al. (2020); Rosotti et al. (2021). The proposed radial locations of two Jupiter-mass planets (one at 15 au and another at 110 au) in the HD 100546 disk inferred from the smoothed-particle-hydrodynamic simulations of Fedele et al. (2021) are shown in purple.

surface of the HD 100546 disk is coincident with the inner edge of a wide (∼40-150 au) continuum gap (Pineda et al. 2019; Fedele et al. 2021). In CI Tau, the vertical dip in CO emitting heights also aligns with a mm dust ring. A similar vertical dip around 50 au is seen in the ^{13}CO J=3–2 emission surface of this disk as modeled by Rosotti et al. (2021). This is consistent with previous observations showing that vertical substructures often occur at a similar radius in multiple CO isotopologues (Law et al. 2021a). In DoAr 25, the B86 dust ring (Huang et al. 2018) lies at the same location as the change in emission surface slope. Similarly, the slope change in CI Tau is at approximately the same radii as a mm dust ring (Clarke et al. 2018; Long et al. 2018).

All sources with vertical substructure in their emission surfaces also have evidence for kinematic planetary signatures (KPSs). Pinte et al. (2020) reported localized deviations from Keplerian rotation, i.e., velocity "kinks," in the GW Lup, WaOph 6, and DoAr 25 disks that were inferred directly from individual CO channel maps. Although we do not identify any definitive substructures in the GW Lup and WaOph 6 disks, both show tentative dips at the same radial locations as the proposed planets. We find no corresponding feature in the CO emission surface of the DoAr 25 disk but note the tentative nature of the KPS in this source (Pinte et al. 2020). In the CI Tau disk, Rosotti et al. (2021) identified a similar kinematic signature with a possible planetary origin at 1.″3 (≈210 au). However, this feature is close to the maximum radius at at which we could constrain the CO emission surface and where the SNR is considerably lower. This results in large vertical scatter beyond ≈150 au and precludes any conclusions about the presence of vertical substructures at large radii. In this disk, Clarke et al. (2018) also proposed that the annular continuum gaps - one of which aligns with the vertical dip at 50 au - are due to three Jupiter-mass planets. Since these inferences were based on dust and gas hydrodynamical simulations, it is possible that the other two gaps are, in fact, planetary in origin but do not produce vertical perturbations in the CO line emission surfaces that are detectable with our current data quality. In the HD 100546 disk, a KPS in the form of a Doppler flip was identified at ≈0.″2-0.″3, or ≈20-30 au (Casassus & Pérez 2019; Pérez et al. 2020). While we find a smoothly varying CO emission surface at these radii, a relatively wide vertical dip is present in the emitting heights a few tens of au exterior to this KPS. The proposed locations of two Jupiter-mass planets, one at 15 au and another at 110 au, from the smoothed-particle-hydrodynamical

simulations (Fedele et al. 2021; but see Pyerin et al. 2021 for alternate predictions of planet radial locations at 13 au and 143 au) are located at the inner and outermost edges, respectively, of where we constrained the CO emission surface. Similar to the KPS in the CI Tau disk, we are unable to determine if any corresponding vertical substructures are present in HD 100546 at or near these radii.

3.3. *Comparison with NIR Scattering Surfaces*

The vertical distribution of micron-sized dust grains in disks should be related to the gas environment, due to strong coupling between small dust and gas. However, few independent height measurements of both small dust grains and line emission surfaces exist in protoplanetary disks (e.g., Dutrey et al. 2017; Villenave et al. 2020; Rich et al. 2021; Law et al. 2021a; Flores et al. 2021; Villenave et al. 2022) but are critical in probing disk characteristics such as gas-to-dust ratios and turbulence levels.

Many disks in our sample have been observed in scattered light (Benisty et al. 2010; Avenhaus et al. 2014; Garufi et al. 2016; Avenhaus et al. 2018; Sissa et al. 2018; D'Orazi et al. 2019; Garufi et al. 2020; Maucó et al. 2020; Brown-Sevilla et al. 2021; Garufi et al. 2022), which provides information about the distribution of micron-sized dust grains. The MY Lup and V4046 Sgr disks have well-defined rings in the NIR with direct estimates of scattering heights (Avenhaus et al. 2018; D'Orazi et al. 2019). The high inclination of the DoAr 25 disk also allows for an inference of its NIR surface, despite the absence of NIR substructure in this source (Garufi et al. 2020). In addition, a geometric model of the NIR structure of the HD 100546 disk has been constructed by Sissa et al. (2018).

Figure 5 shows these NIR heights compared to the CO emission surfaces. To enable a more general comparison, we show the CO emission surfaces versus NIR scattering heights previously reported for the IM Lup, HD 163296, and HD 97048 disks (Law et al. 2021a; Rich et al. 2021). We also plot the powerlaw NIR scattering height relation identified in a sample of disks around T Tauri stars as part of the DARTTS-S program (Avenhaus et al. 2018) as a dashed red line in Figure 5 for all sources, except HD 100546, where we instead show the Sissa et al. (2018) relation. We emphasize that the Avenhaus et al. (2018) trend is an average profile meant to illustrate a typical scattered light surface, rather than a detailed fit to each source.

In our sample, the NIR surfaces generally lie either at or below the CO emission surfaces with two exceptions toward larger radii in MY Lup and DoAr 25. The total size of the NIR disk in DoAr 25 is approximately 100 au greater than that of its CO gas disk (Table 5). The NIR height was only inferred at the outer edge (∼300 au) of the NIR disk (Garufi et al. 2020), but still closely follows the Avenhaus et al. (2018) trend and if extrapolated to smaller radii, lies at the same height as CO. A similar result is found for MY Lup, where the NIR height at ≈120 au is nearly twice as high as that of CO, but if extrapolated to within 100 au, the surfaces agree nearly exactly.

The fact that the small dust grain disk size is larger than the CO line emission extent in DoAr 25 is particularly interesting and at first difficult to reconcile. It is possible that this is an observational bias from insufficient line sensitivity, which might have led to a nondetection of low intensity, large radii CO emission in this disk. If, instead, there is truly little-to-no gas at 300 au, it is not clear how small dust grains are lofted to and maintained at such large heights (≈72 au) without gas pressure support. At this distance, CO may be entirely frozen out, making CO line emission a poor tracer of the gas density at these large radii. The derived temperatures in the outer disk (see Section 3.4) are close to those expected for CO freeze-out to occur and in the absence of significant CO non-thermal desorption, might explain these observations. Alternatively, this discrepancy in scattered light and line emission sizes may be an indication of a wind that is entraining the small dust as it leaves the disk. Deeper CO line observations of the DoAr 25 disk are required to confirm its true CO line emission radial extent and the underlying gas density distribution.

In the HD 163296 and IM Lup disks, Rich et al. (2021) and Law et al. (2021a) found that the CO emission surfaces were considerably more elevated than the NIR heights, with the scattering surfaces typically occupying similar heights as the ^{13}CO emission surfaces (Law et al. 2021a). The 330 au ring seen in HST coronagraphic imaging is an exception to this trend, and instead lies at nearly the same height as the CO line emission. In the HD 97048 disk, the CO and NIR surfaces were initially thought to lie at the same height (Rich et al. 2021), but after re-deriving the emission surfaces (Appendix C), we find that the NIR surfaces lie closer to the ^{13}CO emission surfaces, with the caveat that the uncertainties in CO emitting heights are large due to the coarse beam size (≈0.″45). For completeness, we also plot the outer two NIR rings in HD 97048, which were only detected via Angular Differential Imaging (Ginski et al. 2016), but were not considered in Rich et al. (2021) due to concerns that ADI reduction techniques may alter the

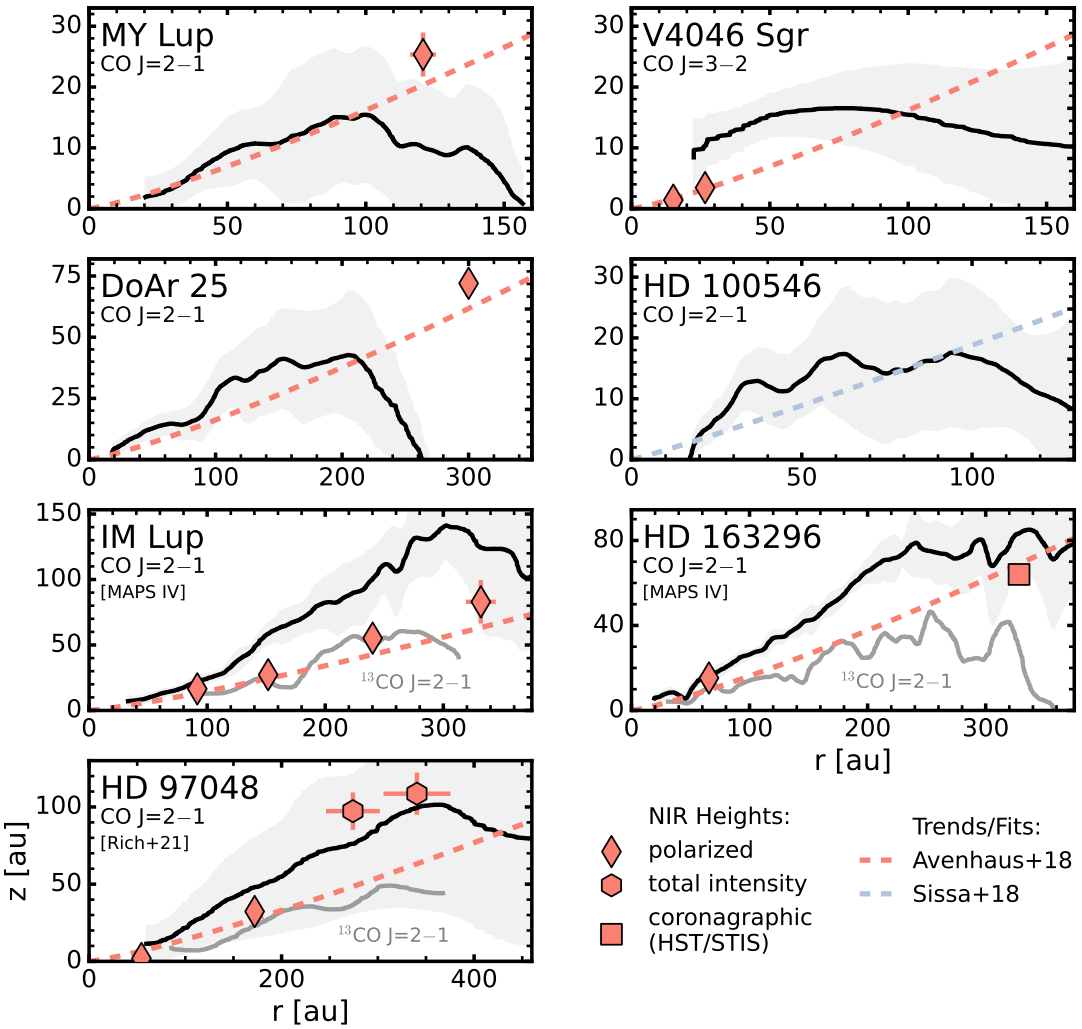

Figure 5. CO emission surfaces for sources in our sample (MY Lup, V4046 Sgr, DoAr 25, HD 100546) and from the literature (HD 163296, IM Lup, HD 97048) versus NIR heights. The black lines are the moving average surfaces and gray shaded regions show the 1σ uncertainty. The red markers show individual height measurements of NIR rings for MY Lup and V4046 Sgr (Avenhaus et al. 2018; D'Orazi et al. 2019); IM Lup and HD 163296 (Monnier et al. 2017; Muro-Arena et al. 2018; Avenhaus et al. 2018; Rich et al. 2020); and HD 97048 (Ginski et al. 2016; Rich et al. 2021), or from the opening angle at the last scattering separation for DoAr 25 (Garufi et al. 2020). Marker types indicate measurements from polarimetric (diamond), total intensity (hexagon), and coronagraphic imaging (square). The red dashed line shows the inferred NIR surface using the powerlaw relation found in a sample of disks in Avenhaus et al. (2018). The blue dashed line shows the geometric scattered light model of the HD 100546 disk from Sissa et al. (2018). The errorbars are smaller than the marker for the rings in V4046 Sgr, while uncertainties are not reported for the NIR measurement in DoAr 25. Light gray curves show the ^{13}CO J=2–1 emission surfaces in the IM Lup and HD 163296 (Law et al. 2021a) and HD 97048 disks (Appendix C).

shape of continuous objects. The heights of these outer rings are comparable to that of the CO emission surface.

Taken together, our results suggest a greater diversity in CO line emission-to-small-dust heights than previously observed with the caveat that NIR and line emission surfaces are not necessarily tracing the same properties in the outer disk regions. It is nonetheless interesting to note that unlike in the inner disks, the NIR heights at large radii are often either comparable to or larger than the CO line emission heights. Higher spatial resolution CO line observations of disks with known NIR features would enable more robust comparisons between the small dust and line emission heights.

3.4. *Gas Temperatures*

CO line emission is expected to be optically thick at typical disk temperatures and densities (e.g., Weaver et al. 2018). Assuming the emission fills the beam and is in local thermodynamic equilibrium, the peak surface brightness I_ν provides a measure of the temperature of the emitting gas. Thus, we can use the line brightness

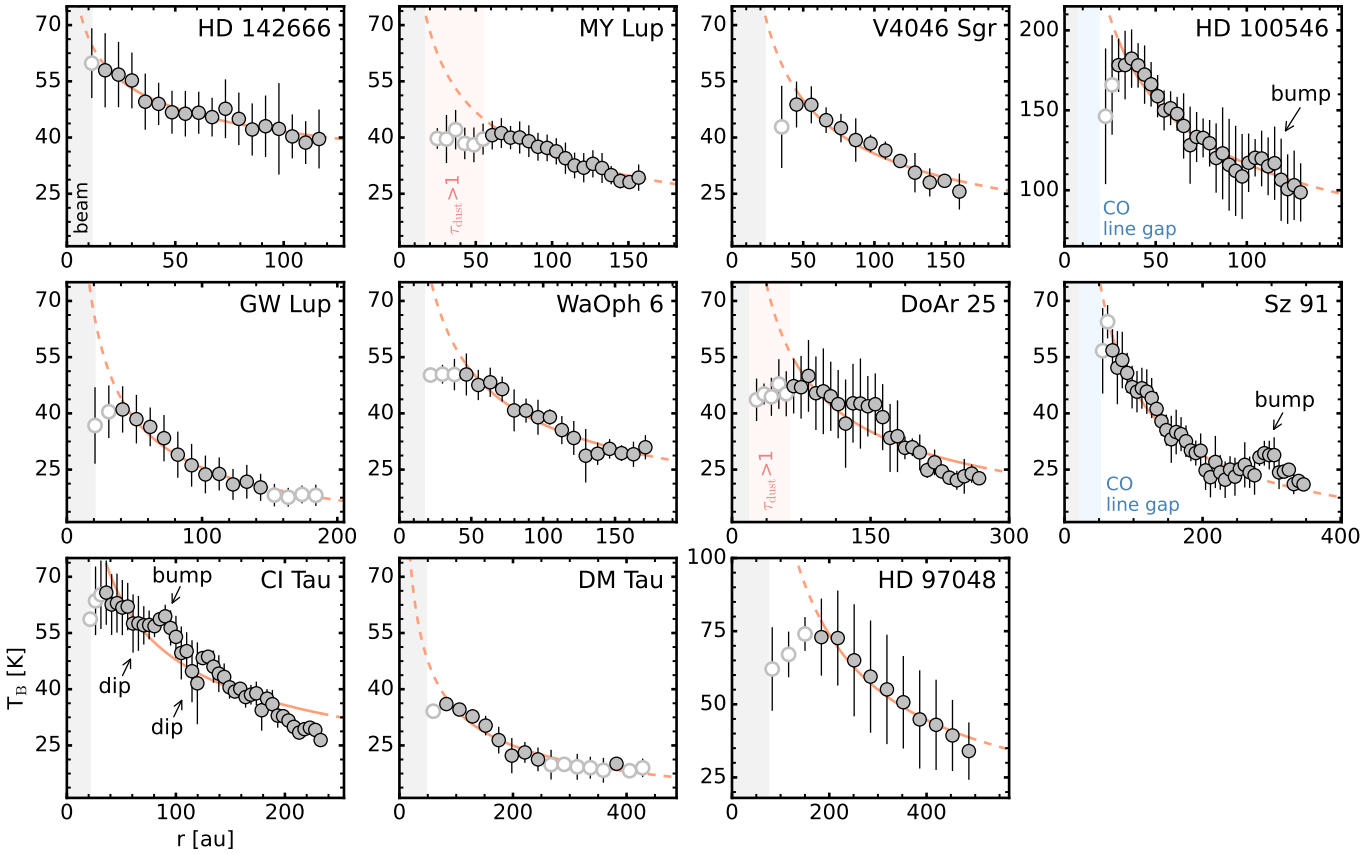

Figure 6. CO radial brightness temperature profiles. These profiles represent the mean temperatures computed by radially binning the individual measurements, similar to the procedure used to compute the radially-binned surfaces (see Section 3.4). Vertical lines show the 1σ uncertainty, given as the standard deviation of the individual measurements in each bin. The solid red lines show the radial range used in the power law fits from Table 3, while the dashed lines are extrapolations. Temperature measurements affected by dust optical depth, beam dilution, or those below 20 K are marked by hollow markers and are not used in the power law fits. The inner gray shaded region is the FWHM of the beam major axis. Regions of optically thick 1.25 mm continuum emission (Huang et al. 2018) are shaded in light red in MY Lup and DoAr 25, while the locations of CO line emission gaps in HD 100546 and Sz 91 (Figure 14) are shaded in blue. Temperature bumps are labeled in HD 100546, Sz 91, and CI Tau with arrows, as are two dips in CI Tau. All panels show a consistent temperature range, except for the HD 100546 and HD 97048 disks, which are considerably warmer than the other sources.

temperatures of the extracted emission surfaces to map the disk thermal structure.

3.4.1. *Calculating Gas Temperatures*

As a first step, we reran the surface extraction procedure on the line+continuum image cubes to not underestimate the line intensity along lines of sight containing strong continuum emission (e.g., Boehler et al. 2017). For each of the pixels extracted, we obtained a corresponding peak surface brightness and then used the full Planck function to convert I_ν to a brightness temperature, which we assumed is equal to the local gas temperature. We emphasize that all subsequent radial and 2D gas temperature distributions represent those derived directly from these individual surface measurements, i.e., pixels where we were able to determine an emission height.

Several of the disks in our sample suffer from foreground cloud contamination (Table 1). To avoid underestimating peak brightness temperatures, we manually excluded all channels with cloud obscuration when refitting the line+continuum surfaces. In addition to our sample, we include the HD 97048 disk in the following analysis. While this disk has a previously mapped CO emission surface (Rich et al. 2021), it lacks an empirical estimate of its CO temperature structure.

3.4.2. *Radial and Vertical Temperature Profiles*

Figure 6 shows the CO radial temperature distributions along the emission surface for all disks. Temperatures range from $\lesssim$20 K (DM Tau) to a maximum of 180 K (HD 100546). Derived brightness temperatures are generally consistent with expectations based on stellar luminosity and spectral classes, with the disks

Table 3. CO Radial Temperature Profile Fits

Source	Line	$r_{fit,in}$ [au]	$r_{fit,out}$ [au]	T_{100} [K]	q	Feat.[a]
HD 142666	J=2−1	18	116	42 ± 0.5	0.20 ± 0.01	
MY Lup	J=2−1	61	157	35 ± 0.3	0.41 ± 0.03	
V4046 Sgr	J=3−2	45	160	36 ± 0.7	0.49 ± 0.04	
HD 100546	J=2−1	30	130	116 ± 1.4	0.42 ± 0.02	B110
GW Lup	J=2−1	41	143	26 ± 0.5	0.60 ± 0.04	
WaOph 6	J=2−1	47	171	37 ± 0.6	0.47 ± 0.03	
DoAr 25	J=2−1	67	268	44 ± 1.1	0.54 ± 0.05	
Sz 91	J=3−2	69	250	47 ± 0.7	0.70 ± 0.03	B300
CI Tau	J=3−2	36	233	48 ± 0.7	0.42 ± 0.03	D70,B90,D120
DM Tau	J=2−1	83	382	34 ± 1.0	0.47 ± 0.05	
HD 97048	J=2−1	184	487	122 ± 7.8	0.72 ± 0.06	

[a]Local temperature bumps (B) or dips (D) labeled according to their approximate radial location in au.

around Herbig Ae/Be stars HD 142666, HD 100546, and HD 97048 showing warmer temperatures than most of the T Tauri stars. Among the disks around T Tauri stars, there are modest temperature variations. For instance, the disk around Sz 91 is 1.3-1.5× warmer than that around DM Tau at the same radii, despite both being transition disks with similar host stellar luminosities. However, the central cavity of the Sz 91 disk is much larger than that of DM Tau (Andrews et al. 2011; Canovas et al. 2015; Kudo et al. 2018; Maucó et al. 2020), which results in increased irradiation at large radii and likely contributes to this temperature difference. Moreover, we find that the derived temperatures in DM Tau are consistent with those inferred in the parametric forward models of Flaherty et al. (2020), which account for beam smearing. This suggests that the temperatures derived here are not substantially lowered by non-unity beam filling factors, despite the DM Tau data having a relatively coarse beam size.

A drop or flattening in brightness temperature is seen interior to 20–50 au in all disks, which is marked as a gray shaded region in Figure 6. At the smallest radii, this is primarily due to beam dilution as the emitting area becomes comparable to or smaller than the angular resolution of the observations. However, for the MY Lup, HD 100546, WaOph 6, and DoAr 25 disks, the central temperature dip or plateau extends further than the beam size. There are several explanations for this: CO is depleted enough for the lines to become optically thin at these radii, the presence of unresolved CO emission substructure, or a substantial fraction of the CO emission is absorbed by dust. The dip in the HD 100546 disk is likely due to the inner CO line emission gap (Figure 1), which results in the emission becoming less optically thick within 1/2-1 beams of the gap edge and thus no longer measures the gas temperature. The inner disks of MY Lup and DoAr 25 show optically thick dust (Huang et al. 2018) and the radii where $\tau_{1.25\,mm} > 1$ are similar to where the derived CO temperature begins to plateau. WaOph 6, however, does not exhibit optically thick dust in its inner disk, but shows hints of additional CO line emission substructure in the form of a low-contrast dip at small radii, as seen in its radial profile in Figure 14. Higher angular resolution CO line observations toward this disk are necessary to confirm the reality of this dip and the presence of any additional chemical substructures.

Next, we fitted the temperature profiles with power law profiles, parameterized by slope q and T_{100}, the brightness temperature at 100 au, i.e.,

$$T = T_{100} \times \left(\frac{r}{100\,\mathrm{au}}\right)^{-q}. \quad (2)$$

For derived brightness temperatures less than 20 K – below the CO freeze-out temperature – the associated line emission is at least partially optically thin and thus only provides a lower limit on the true gas temperatures. We exclude all temperatures <20 K in our fits, as well as those affected by beam dilution or dust optical depth, as discussed above (also see Figure 6). We also manually excluded the temperature bump at large radii in the Sz 91 disk. We then fitted each profile using the Levenberg-Marquardt minimization implementation in `scipy.optimize.curve_fit`. Table 3 lists the fitting ranges and derived parameters. As shown in Figure 6, most sources are well fitted by power law profiles and with $q \approx 0.4$-0.6, while HD 142666 has a considerably

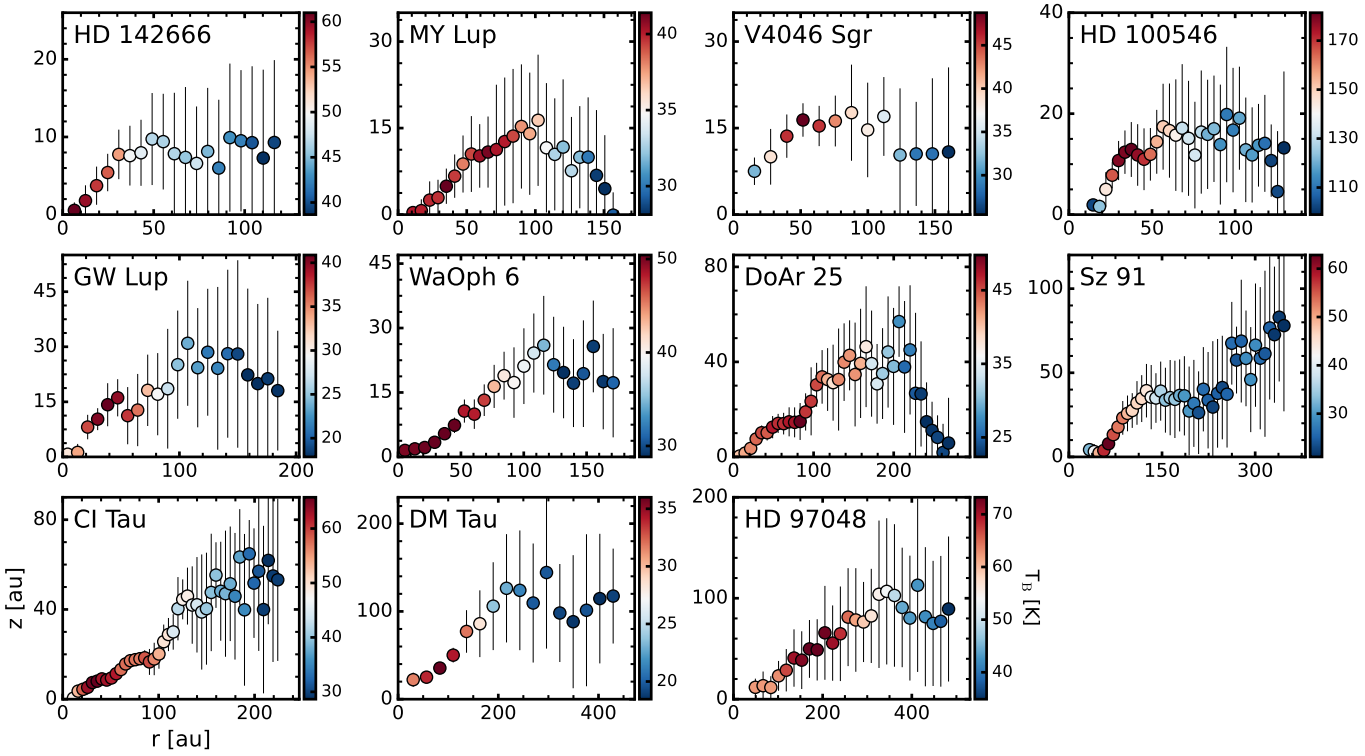

Figure 7. 2D temperature distributions of CO emission surfaces in all disks. Points are those from the binned surfaces and error bars are the 1σ uncertainties in z. For some of the innermost points, the uncertainty is smaller than the marker. The uncertainty of the temperature measurements, which is not shown here, can be seen in Figure 6. The 2D temperature profiles shown in this figure are available as Data behind the Figure.

shallower ($q = 0.20$) profile, and Sz 91 and HD 97048 are steeper ($q = 0.70$-0.72).

Instead of showing the derived temperature profiles as only a function of radius as in Figure 6, we can also map out full 2D temperature profiles. Figure 7 shows the thermal structure of the CO emitting layer as a function of (r, z) for each source.

3.5. *Temperature Substructures*

While the temperature profiles are in general quite smooth, three sources show local dips or bumps in temperature. The HD 100546 and Sz 91 disks show temperature bumps at 110 au and 300 au, respectively, while the CI Tau disk shows a more complex structure with two dips at 70 au and 120 au and a bump at 90 au. For this 90 au feature in CI Tau, we are unable to distinguish if this is simply a local maximum resulting from the adjacent dips, or if this is a true temperature enhancement. Each of these features is catalogued in Table 3.

For these three sources, we checked for possible spatial links with known millimeter dust features, as local temperature deviations in disks are sometimes found at the locations of dust rings or gaps (e.g., Facchini et al. 2018; van der Marel et al. 2018; Calahan et al. 2021).

In HD 100546, the 110 au temperature bump is located at the center of a wide dust gap between the bright inner ring (20-40 au) and the faint outer ring (150-250 au) (Walsh et al. 2014; Pyerin et al. 2021). Recent modeling suggests a 8.5 M_{Jup} planet at 110 au (see Figure 4) and predicts locally diminished gas and mm dust surface densities (Fedele et al. 2021). Pyerin et al. (2021) instead find evidence of a 3 M_{Jup} planet at 143 au, which places the temperature bump interior to, and not radially coincident with, the proposed planet location.

In Sz 91, the temperature bump at 300 au is well beyond the mm dust ring at 90 au (Canovas et al. 2016; Maucó et al. 2020) and corresponds to the low-intensity, plateau-like CO emission seen at large radii (Figure 14). A similar temperature bump was identified in the outer disk of IM Lup (Law et al. 2021a) and is thought to be the result of a midplane temperature inversion (Cleeves 2016; Facchini et al. 2017) or due to a photoevaporative wind (Haworth et al. 2017).

In CI Tau, the dip at 120 au aligns with a dust gap, while the dip at 70 au lies close to a ^{13}CO line emission gap and continuum ring (Long et al. 2018; Clarke et al. 2018; Rosotti et al. 2021). The 90 au temperature bump

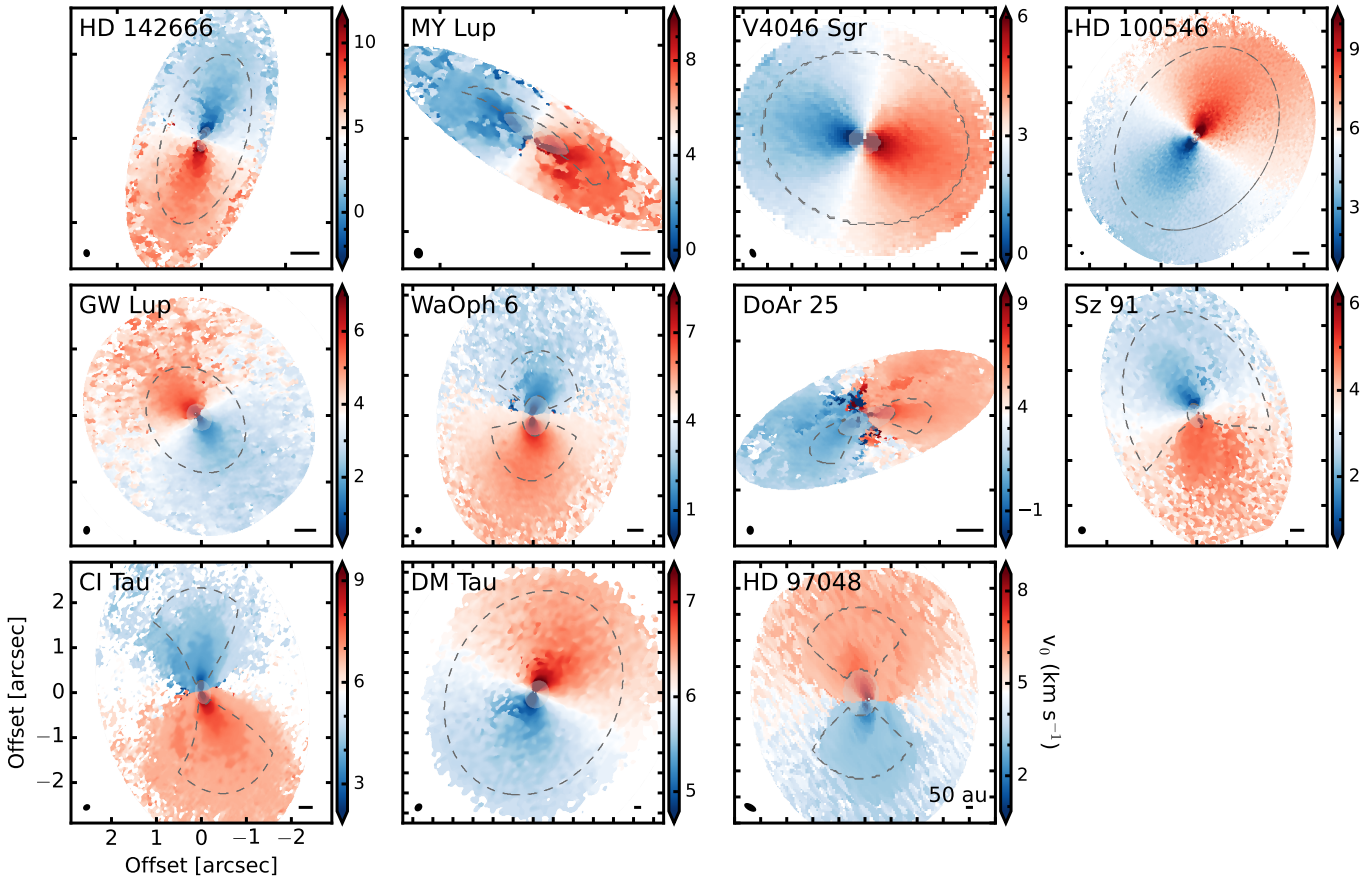

Figure 8. Gallery of rotation maps of CO emission in our disk sample. The innermost few beams, which are excluded from the fits, are shaded, while the outermost fitting radius is marked by a dashed line. For those disks with high inclinations or foreground cloud absorption, the wedges used in the fitting are shown by dashed lines. Each tick mark represents 1″. Velocity signatures from both the front and back sides of the MY Lup and DoAr 25 disks are clearly visible due to the high inclination of these sources. The synthesized beam and a scale bar indicating 50 au is shown in the lower left and right corner, respectively, of each panel.

is coincident with a pronounced change in the emission surface slope and also close to mm dust ring.

3.6. *Dynamical Masses*

We used CO rotation maps to derive dynamical masses for all sources in our sample, closely following the methods of Teague et al. (2021). We first used the 'quadratic' method of `bettermoments` (Teague & Foreman-Mackey 2018) to produce maps of the line center (v_0), which includes a statistical uncertainty for v_0. The rotation maps were then masked to only include regions where the peak intensities are greater than five times the RMS value measured in a line free channel to remove noisy values at the disk outer edges.

We fitted the resulting rotation maps with `eddy` (Teague 2019a), which uses the `emcee` (Foreman-Mackey et al. 2013) python code for MCMC fitting. We consider five free parameters in modeling the Keplerian velocity fields: the source offset from phase center (δx, δy), disk position angle (PA), host star mass (M_*), and systemic velocity (v_{lsr}). The disk inclination (i) and emission surfaces, parameterized by z_0, ϕ, r_{taper}, and ψ (Equation 1), were held fixed. For each disk, the innermost 2-4 beams, depending on the source, were masked to avoid confusion from beam dilution. The outermost radii were set by a combination of SNR and the desire to avoid contamination from the rear side of the disk. Table 4 provides the selected values. The uncertainty maps produced by `bettermoments` were adopted as the uncertainties during the fitting.

We used 64 walkers to explore the posterior distributions of the free parameters, which take 500 steps to burn in and an additional 500 steps to sample the posterior distribution function. The posterior distributions were approximately Gaussian for all parameters with minimal covariance between other parameters. Thus, we took model parameters as the 50th percentiles, and the 16th to 84th percentile range as the statistical uncer-

Table 4. Best Fit CO v_{kep} Models

Model		HD 142666	MY Lup[a]	V4046 Sgr	HD 100546	GW Lup	WaOph 6[b]	DoAr 25[a,b]	Sz 91[b]	CI Tau[b]	DM Tau	HD 97048[b]
Parameter		J=2−1	J=2−1	J=3−2	J=2−1	J=2−1	J=2−1	J=2−1	J=3−2	J=3−2	J=2−1	J=2−1
δx_0	(mas)	−49 ± 2	−106 ± 3	−84 ± 5	−13 ± 1	−29 ± 5	−275 ± 3	[38][c]	−443 ± 4	−4 ± 1	19 ± 8	19 ± 7
δy_0	(mas)	38 ± 3	90 ± 2	−974 ± 5	−6 ± 1	6 ± 5	−341 ± 5	[−494][c]	−872 ± 4	9 ± 1	−21 ± 10	378 ± 15
i	(°)	[−62.2]	[−73.2]	[34.7]	[−41.7]	[−38.7]	[−47.3]	[67.4]	[49.7]	[−49.2]	[36.0]	[−41.0]
PA	(°)	161.2 ± 0.29	238.4 ± 0.17	255.6 ± 0.13	323.9 ± 0.05	37.2 ± 0.65	173.5 ± 0.30	289.2 ± 0.36	197.0 ± 0.26	192.7 ± 0.07	334.5 ± 0.24	8.0 ± 0.23
M_*	($M_\odot$)	1.73 ± 0.019	1.27 ± 0.014	1.72 ± 0.008	2.10 ± 0.004	0.62 ± 0.010	1.12 ± 0.008	1.06 ± 0.013	0.55 ± 0.007	1.02 ± 0.001	0.50 ± 0.004	2.70 ± 0.015
v_{LSR}	(km s^{-1})	4.37 ± 0.015	4.71 ± 0.014	2.93 ± 0.003	5.65 ± 0.001	3.69 ± 0.011	4.21 ± 0.006	3.38 ± 0.018	3.42 ± 0.005	5.70 ± 0.002	6.04 ± 0.002	4.55 ± 0.004
z_0	($''$)	[0.09]	[0.21]	[0.28]	[0.35]	[0.22]	[0.37]	[0.31]	[0.91]	[0.32]	[0.82]	[0.88]
ϕ	(-)	[0.50]	[1.28]	[0.59]	[1.09]	[0.76]	[1.77]	[1.54]	[2.59]	[1.48]	[1.85]	[2.86]
r_{taper}	($''$)	[1.13]	[0.80]	[1.99]	[1.02]	[1.22]	[1.13]	[1.61]	[0.86]	[2.07]	[1.79]	[0.86]
ψ	(-)	[2.37]	[3.95]	[2.59]	[2.57]	[5.91]	[2.52]	[5.85]	[1.99]	[2.61]	[1.67]	[1.10]
d	(pc)	[145.4]	[156.7]	[71.3]	[108.0]	[154.1]	[122.4]	[137.7]	[157.9]	[160.2]	[143.1]	[183.9]
$r_{fit,in}$	($''$)	[0.15]	[0.40]	[0.65]	[0.15]	[0.22]	[0.50]	[0.40]	[0.28]	[0.27]	[0.72]	[0.90]
$r_{fit,out}$	($''$)	[1.05]	[0.91]	[4.28]	[2.77]	[0.86]	[1.62]	[0.86]	[2.38]	[2.31]	[5.26]	[3.27]

NOTE—Uncertainties represent the 16th to 84th percentiles of the posterior distribution. Values in brackets were held fixed during fitting.

[a] Due to high disk inclinations, fits performed using manually-drawn wedges to avoid including the back side of the disk.

[b] Wedge sizes and fitting radii were manually adjusted to avoid cloud obscured regions.

[c] R.A. and Dec. positional offsets fixed to those derived from continuum fitting (Huang et al. 2018).

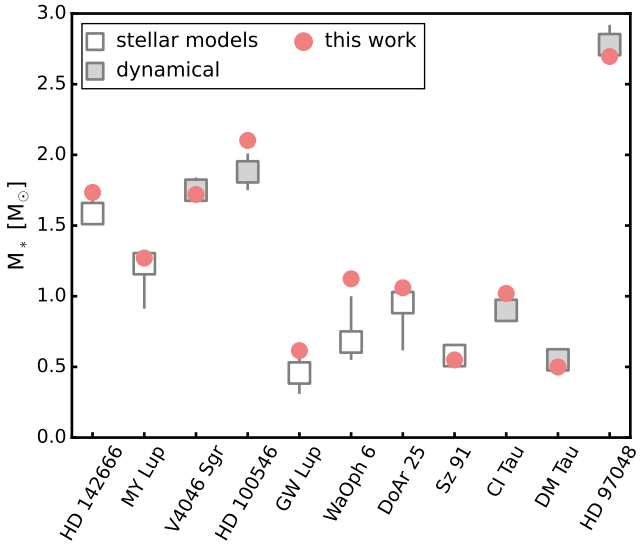

Figure 9. Comparison of literature stellar masses (squares) and those derived in this work (circles). Dynamical masses are shown as filled markers while those from stellar models are hollow. The errorbars are smaller than the marker for several sources. The references for literature masses are: HD 142666, MY Lup, GW Lup, WaOph 6, DoAr 25 (Andrews et al. 2018); V4046 Sgr (Rosenfeld et al. 2012); HD 100546, HD 97048 (Casassus & Pérez 2019); Sz 91 (Maucó et al. 2020); CI Tau (Simon et al. 2017, 2019); and DM Tau (Simon et al. 2019).

tainties. Table 4 lists the fitted values and uncertainties for all disks.

For disks with foreground cloud absorption, we restricted the fitting regions by using manually selected wedges. The high inclination of MY Lup and DoAr 25 results in the presence of conspicuous velocity signatures from the back side of the disk. To avoid confusion in the fitting, we also excluded these regions in both disks. Figure 8 shows all rotation maps and the fitting regions used in `eddy`.

Figure 9 shows the derived dynamical masses versus literature values, compiled from both dynamical- and stellar evolutionary model-based estimates. In general, we find excellent agreement with previous measurements, with the exception of WaOph 6, where we find a considerably larger mass (≈1.1-2.0×) than reported in Andrews et al. (2018). This difference may reflect the uncertainty of stellar evolutionary models in inferring the masses of low-mass pre-main-sequence stars (e.g., Simon et al. 2019; Pegues et al. 2021), or alternatively, indicate that the spectral type is underestimated by 1-2 subclasses, i.e., WaOph 6 may be a K4/K5-type star instead of K6.

4. DISCUSSION

4.1. *Comparison with Previous Results*

The CO emission surfaces of three of our disks have been presented in previous publications using several different methods but with the same data sets as in this work. It is therefore useful to compare their results with ours.

4.1.1. *HD 100546*

Casassus & Pérez (2019) found a CO emission height[2] of z/r≈0.16 between 0.″15-0.″75 (17-83 au) by fitting the CO J=2–1 rotation map, i.e., using deviations from Keplerian velocity to infer an emission surface. In this same region, we find $z/r \approx$ 0.25-0.3, a factor of two greater than their estimate. We can think of two possible explanations for this discrepancy: (1) The surface begins to flatten and turnover at 0.″60 (≈65 au), and Casassus & Pérez (2019) may have weighted this part of the disk in their fit more than we did, resulting in an overall lower z/r, i.e., at 0.″75 we find z/r≈0.18. (2) We identify a vertical dip at 45 au (Section 3.2) in the emission surface, which will lower the average z/r.

4.1.2. *CI Tau*

Rosotti et al. (2021) found $z/r \approx 0.3$ for the CO J=3–2 emission height, which was visually determined by overlaying conical surfaces onto moment maps of CI Tau. Overall, this is quite consistent with what we derive, with the caveat that we find a flaring surface such that interior to 90 au, the slope is shallower with $z/r \approx$ 0.2-0.25, while beyond 90 au, it is $z/r \approx 0.3$.

4.1.3. *DM Tau*

Flaherty et al. (2020) modeled CO line observations in DM Tau and extracted the resulting CO J=2–1 line emission heights (see their Figure 2). In the inner, flared region of the surface, Flaherty et al. (2020) estimated $z/r \sim 0.4$, while we found $z/r \gtrsim 0.5$. Beyond 250 au, once the surface begins to plateau, both our directly-mapped surfaces and the modeled emission surfaces lie at roughly the same vertical heights. Thus, we find in general, good agreement between the two approaches.

4.2. *Origins of CO Emission Surface Heights*

Given the observed diversity in CO emitting heights, we explore possible mechanisms which may set the vertical extent and degree of flaring in line emission surfaces in the following subsections. We examine trends in emission surface heights with physical characteristics of our

[2] The authors fitted the opening angle $\psi = \arctan(z/r)$ above the disk midplane and found $\psi = 9°.3 \pm 2°.5$, which is equal to $z/r \approx 0.16 \pm 0.04$.

sources in Section 4.2.1 and present possible explanations for the observed correlations in Section 4.2.2.

4.2.1. *Correlations with Source Characteristics*

We expect that source physical characteristics will influence line emission surfaces. As part of MAPS, Law et al. (2021a) found that protoplanetary disks with lower host star masses, cooler temperatures, and larger CO gas disks had CO emission surfaces with higher z/r values. However, these trends were tentative, given the small sample size of five disks. Garufi et al. (2021) also reported a positive trend between disk size and H_2CO line emitting heights in five Class I disks in the ALMA-DOT survey. This suggests that this trend may extend to earlier phases of disk evolution and may hold for other molecules besides CO, but firm conclusions were again limited by the small sample size. To test the robustness of these trends, we combine our disk sample with the five MAPS disks (Law et al. 2021a) and the HD 97048 disk (Rich et al. 2021), which both have CO emission surfaces mapped in the same way.

We first require stellar masses, gas temperatures, and CO gas disk sizes for all sources to enable a homogeneous comparison. We derived dynamical masses (Section 3.6) and gas temperatures (Section 3.4) for the disks in our sample, while the MAPS disks have existing dynamical masses and CO gas temperatures, which were derived in a consistent way from Teague et al. (2021) and Law et al. (2021a), respectively. We also computed the CO gas sizes (R_{CO}) of each disk, as defined by the radius which contained 90% of total line flux (e.g., Tripathi et al. 2017; Ansdell et al. 2018). This definition is consistent with that used in Law et al. (2021b) and allows us to easily compare with the CO gas disk sizes of the MAPS sources. Table 5 shows the resulting CO sizes and Appendix A provides additional details of this calculation.

Each emission surface spans a range of z/r values, e.g., flaring, plateau/turnover, vertical substructures, but for source-to-source comparisons, we wish to determine a characteristic z/r. We choose to focus on the inner regions of the disk where CO emission heights are sharply rising and to exclude the outer disks where the emitting surfaces plateau or turnover. We define the characteristic z/r of each CO emission surface as the mean of all z/r values interior to a cutoff radius of $r_{\rm cutoff} = 0.8 \times r_{\rm taper}$, where $r_{\rm taper}$ is the fitted parameter from the exponentially-tapered power law profiles from Table 2. We chose 80% of the fitted $r_{\rm taper}$ to ensure that we only included the rising portion of the emission surfaces and visually confirmed that this choice was suitable for all sources (Figure 17). As some disks are considerably more flared than others, i.e., z/r changes rapidly with radius, we also computed the 16th to 84th percentile range within these same radii as a proxy of the overall flaring of each disk. We applied this same definition to the MAPS disks (Law et al. 2021a) and the HD 97048 disk (Rich et al. 2021) to compile consistent characteristic z/r values. For further details and a list of all z/r values, see Appendix D.

Figure 10 shows these representative z/r values as a function of stellar host mass, mean gas temperature, and CO gas disk size. With this larger disk sample, emission surface heights show a weak decline with both host stellar mass and CO gas temperature. These trends show a high degree of scatter but are broadly consistent with the trends previously seen in Law et al. (2021a). We return to these in the following subsection.

We also find that R_{CO} and z/r are strongly correlated. To quantify this correlation, we employ the Bayesian linear regression method of Kelly (2007) using the `linmix` python implementation.[3] We find a best-fit relation of $z/r = (3.6 \pm 0.7 \times 10^{-4})\ R_{CO} + (0.11 \pm 0.03)$ with a 0.06 scatter of the correlation (taken as the standard deviation σ of an assumed Gaussian distribution around the mean relation). We find a correlation coefficient of $\hat{\rho} = 0.83$ and associated confidence intervals of (0.44, 0.99), which represent the median and 99% confidence regions, respectively, of the 2.5×10^5 posterior samples for the regression. Figure 10 shows the derived relationship.

In addition to those sources considered here, we also plot the following literature sources in Figure 10 as hollow squares: HD 169142, V892 Tau, HD 135344B (SAO 206462), IRAS 04302+2247, Flying Saucer (2MASS J16281370-2431391), Oph 163131 (SSTC2D J163131.2-242627), and Gomez's Hamburger (GoHam, IRAS 18059-3211). HD 169142 is an isolated Herbig Ae/Be star hosting a protoplanetary disk with a CO emission height of $z/r = 0.26$ derived from the thermo-chemical models of Fedele et al. (2017). V892 Tau is binary system with two near-equal mass A stars hosting a circumbinary disk with a CO emitting height of $z/r \sim 0.1$ inferred directly from channel maps (Long et al. 2021), while HD 135344B is an F-type star hosting a transition disk with $z/r = 0.27^{+0.19}_{-0.08}$, as derived from rotation curve fitting (Casassus et al. 2021). We measured R_{CO} from the radial profiles of HD 169142 (Yu et al. 2021) and HD 135344B (Casassus et al. 2021) (see Appendix A), while V892 Tau already had a R_{CO} estimate made in a consistent way from

[3] https://github.com/jmeyers314/linmix

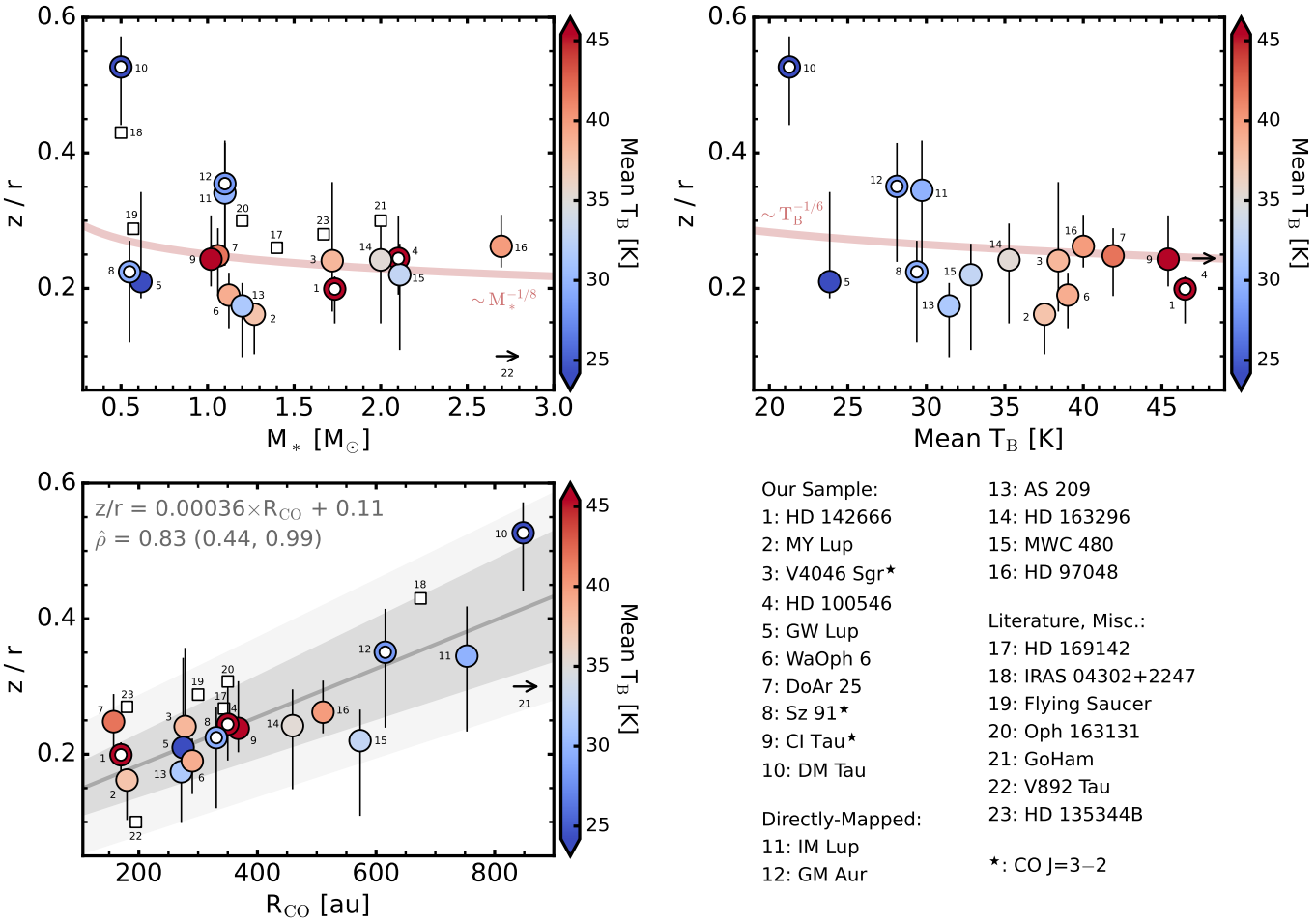

Figure 10. Characteristic z/r of CO emission heights versus stellar mass (top left), mean CO gas temperature (top right), and CO gas disk size (bottom). All masses are derived dynamically (Section 3.6), mean CO gas temperature are computed over the same radial range in which z/r is determined, and gas disk sizes are computed as the radius containing 90% of total flux (Appendix A). Annular markers indicate transition disks. All points are colored by the mean CO gas temperature. Vertical lines show the 16th to 84th percentile range. Approximate scaling relations for stellar mass and temperature are shown as solid red lines. For the z/r-R_{CO} panel, the derived relation is marked with a solid grey line and the 68% confidence interval is shown as the dark grey shaded region. The light grey shaded region denotes the scatter around the mean relation. Literature sources without directly-mapped emission surfaces are shown as hollow squares and include: HD 169142 (Fedele et al. 2017; Yu et al. 2021); IRAS 04302+2247 (Podio et al. 2020); Flying Saucer (Dutrey et al. 2017; Ruíz-Rodríguez et al. 2021); Oph 163131 (Flores et al. 2021; Villenave et al. 2022); GoHam (Teague et al. 2020); V892 Tau (Long et al. 2021); and HD 135344B (Casassus et al. 2021). All data are CO J=2–1, except for those marked with a star (⋆), which are CO J=3–2.

Long et al. (2021). The Flying Saucer (Dutrey et al. 2017; Ruíz-Rodríguez et al. 2019), Oph 163131 (Flores et al. 2021; Villenave et al. 2022), and GoHam (Teague et al. 2020) are edge-on protoplanetary disks, where the emission surface height can be directly measured. IRAS 04302+2247 is an edge-on, Class I disk taken from the ALMA-DOT sample (Garufi et al. 2021), with an emission surface of $z/r \approx 0.41$-0.45 (Podio et al. 2020). For these latter four sources, their edge-on nature makes measuring comparable R_{CO} values difficult and we instead visually estimate disk sizes from their zeroth moment maps. The CO gas disk size of IRAS 04302+2247 is particularly uncertain due to presence of envelope emission (Podio et al. 2020). All literature sources have existing dynamical mass measurements. Despite their heterogeneous nature, all sources lie closely along the same R_{CO}-z/r trend as our disk sample. If we include the literature sources in the `linmix` fitting as before, the derived R_{CO}-z/r relation remains largely unaltered. Moreover, there do not appear to be any obvious systematic biases affecting emission heights derived from mid-inclination disks versus those inferred directly from edge-on disks.

The GoHam edge-on disk (Teague et al. 2020) is one notable exception to this trend. The CO emission sur-

face[4] is $z/r \sim 0.3$, but the size of the CO gas disk is >1400 au. While one would not necessarily expect the positive R_{CO}-z/r trend to continue linearly to larger CO gas disks, as this would quickly result in unphysical z/r values, the GoHam value is considerably lower than we see for several other large, e.g., 600-900 au-sized, disks. This suggests that there is some additional effect at play. In the case of GoHam, this lower-than-expected z/r may be due to self-gravity at larger disk radii, especially considering parts of the GoHam disk have been show to be marginally gravitationally unstable, with Toomre parameter $Q \lesssim 2$ (Berné et al. 2015). It is also possible that GoHam is truly an outlier in terms of its disk structure. Observations of more disks, particularly those with large CO gas extents, are required to assess this.

4.2.2. *Explaining Emission Surface Height Trends*

Here, we explore if the trends observed in the previous subsection are in line with expectations based on scaling relations or overall disk structure. In assessing the vertical distribution of line emission in disks, we first consider the gas pressure scale height, H_g, which is given by:

$$H_g = \sqrt{\frac{k_B T_{mid} r^3}{\mu m_p G M_*}} \quad (3)$$

where M_* is the stellar mass, T_{mid} is the midplane temperature, k_B is the Boltzmann constant, μ is the mean molecular weight, m_p is the proton mass, and G is the gravitational constant. For the following discussion, we assume that line emission surface heights correlate with H_g, i.e., $z/r \sim H_g$ and the measured CO gas temperatures in Section 3.4 correlate with midplane temperature, i.e., $T_{CO} \sim T_{mid}$. We examine the former assumption in detail in the following subsection and note that while disks have a vertical temperature gradient, as the CO isotopologue data show (Law et al. 2021a), the perturbations of the vertical structure from an isothermal disk are still generally small (e.g., Rosenfeld et al. 2013). Even if the disk atmosphere temperature traced by CO is substantially warmer than the gas temperature in the midplane, we expect them to at least roughly scale with one another.

From Equation 3, line emitting heights scale as $z/r \sim \sqrt{T}/\sqrt{M_*}$. Thus, stellar mass and gas temperature should each contribute in setting the z/r of emission surfaces, with cooler disks and less massive host stars leading to more vertically-extended emission surfaces. However, we do not expect T and M_* to be independent variables and to estimate scaling relationships, we next need to examine the expected dependent of T on M_*.

If $T \sim L_*^{1/4}$, then for any stellar mass-luminosity scaling $L_* \sim M^a$ with $a < 4$, we expect z to weakly decrease with M_*. For instance, if $a = 3$, then $T \sim M^{3/4}$ and we find that $z/r \sim M^{-1/8}$. If we instead consider temperature instead of stellar mass, we find that z/r also scales weakly with T (again, assuming $a < 4$). As above, for $a = 3$, we expect $z/r \sim T^{-1/6}$. Both of these scaling relations are shown in their respective panels in Figure 10. Thus, the weakly declining trends between both z/r and stellar mass and mean CO gas temperature seen in Figure 10 are, to first order, consistent with expectations from these simple scaling relations. However, in contrast to the observed z/r-R_{CO} correlation, these trends remain highly suggestive in nature, especially due to the limited parameter space they span, namely either few or no sources with low (<0.5 $M_\odot$) or high (>3 $M_\odot$) stellar masses or with warmer ($T_B > 50$ K) mean gas temperatures.

We next consider the origins of the strong z/r-R_{CO} correlation observed in the previous subsection. In Figure 11, we show the CO gas disk size versus the cutoff radius, in which the characteristic z/r values were measured (also see Appendix D). We find a positive trend

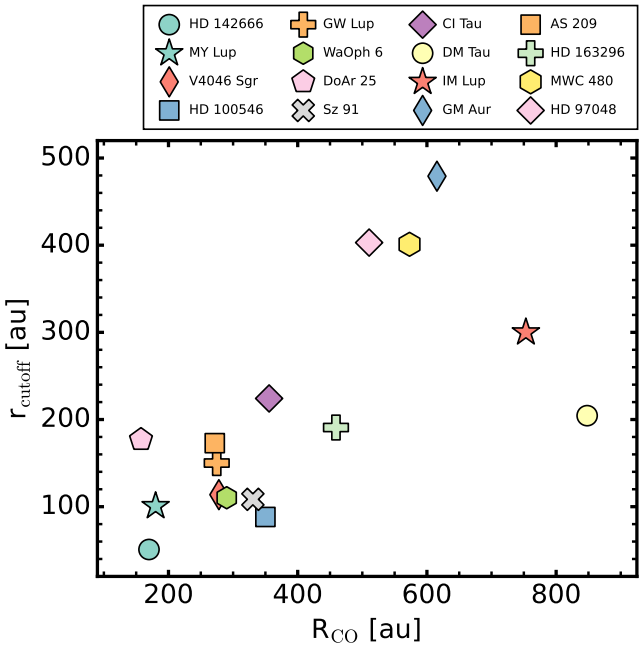

Figure 11. CO gas disk size versus the cutoff radius, interior to which characteristic z/r values were measured (see Appendix D).

[4] This z/r may be modestly underestimated due to the coarse angular resolution ($\gtrsim 1''$) of the data from which it was derived (Teague et al. 2020). However, this does not change the outlier nature of GoHam, as z/r would need to be more than a factor of two larger to be consistent with the observed z/r-R_{CO} trend.

between R_{CO} and r_{cutoff}, which suggests that the z/r-R_{CO} correlation is due to the flared nature of disk line emission surfaces. As we are averaging over wider radial ranges, i.e., larger r_{cutoff}, for those disks with larger R_{CO}, we find higher characteristic z/r values. Thus, we expect the z/r-R_{CO} trend seen in Figure 10 to be driven, in large part, by disk flaring.

4.3. *Emission Surfaces and Gas Scale Heights*

Next, we explore the relationship between CO line emission surfaces and gas pressure scale heights.

We adopt the model of H_{gas} from Equation 3. We take M_* from Table 1 and assume $\mu = 2.37$. We approximate the midplane temperature profile using the simplified expression for a passively heated, flared disk in radiative equilibrium (e.g., Chiang & Goldreich 1997; D'Alessio et al. 1998; Dullemond et al. 2001):

$$T_{\rm mid} = \left(\frac{\varphi L_*}{8\pi r^2 \sigma_{\rm SB}}\right)^{0.25} \quad (4)$$

where L_* is the stellar luminosity (Table 1), σ_{SB} is the Stefan-Boltzmann constant, and φ is the flaring angle. For consistency with Huang et al. (2018) and Dullemond et al. (2018), we adopt a conservative $\varphi = 0.02$ for all disks. We note that, if instead, we use the values obtained from our CO emission surfaces and assume that z/r is a perfect tracer of H_g/r, i.e., $\varphi = \psi - 1$, we find a constant offset in H_g by a factor of ≈1.3, or that the CO line emission surface is more vertically extended than the absorption surface. This is sensible, as disks have vertical temperature inversions and thus more gas at $z = H_g$ - and a higher CO $\tau = 1$ emission surface - than expected from a simple Gaussian vertical model.

Figure 12 shows the ratio of the CO emission surfaces and derived H_g as a function of radius, i.e., z/H_g. For the majority of disks, the CO emission surface traces ≈2-5×H_g, which is consistent with previously inferred ratios between CO emitting heights and H_g (e.g., Dartois et al. 2003; Dutrey et al. 2017; Pinte et al. 2018; Flaherty et al. 2020). Some sources show relatively constant ratios over their radial extents, such as WaOph 6 or HD 97048, while others have ratios that vary by up to a factor three, e.g., GW Lup, DM Tau. In a few cases in the innermost radii, the ratio reaches very high values $\gtrsim$8, but this is the region in which it is the most difficult to extract emission surfaces. Thus, such high inner values should be regarded with caution.

To use CO emission surfaces to infer gas pressure scale heights, we need to better understand why the z/H_g ratios are so different both within and among disks. Here, we explore if the difference can be attributed to stellar mass or disk radius. Figure 13 shows the mean z/H_g of each disk versus stellar mass and the CO disk gas size. We find that mean z/H_g weakly declines with stellar mass and shows a positive correlation with R_{CO}. These trends follow those observed in Section 4.2 but exhibit considerably greater scatter. They are likely driven by the emission surface height correlation seen in Figure 10, as higher emission surfaces will result in larger z/H_g ratios and the fact that source-to-source variation in H_g does not exceed a factor of two and for most sources, is often considerably smaller. Overall, this suggests that if one can measure both the CO gas disk size and emission surface for a particular disk, it may be possible to infer its radially-averaged gas pressure scale height.

5. CONCLUSIONS

Using archival ALMA observations of CO J=2–1 and J=3–2 at high spatial resolution, we extracted emission surfaces in a sample of ten protoplanetary disks. We find the following:

1. CO line emission surfaces vary substantially among disks in their heights. Peak emission heights span a few tens of au to over 100 au, while z/r values range from ≈0.1 to $\gtrsim$0.5.

2. A few emission surfaces present substructures in the form of vertical dips or abrupt slope changes. All of these features align with known millimeter dust substructures.

3. We compare the heights of micron-sized dust grains and CO line emission for those disks with well-constrained NIR scattering heights. CO-to-small-dust heights are quite diverse, with CO emitting heights being higher than the NIR scattering surfaces in some sources, while in others, such as the MY Lup and DoAr 25 disks, the NIR heights are more elevated than the CO line emission. The radial extent of the DoAr 25 disk in scattered light is nearly 100 au larger than in CO line emission, which may be due to insufficient line sensitivities, the presence of a wind, or CO freeze-out at large radii.

4. We derive radial and vertical temperature distributions in CO for all disks. Temperatures are generally consistent with source spectral types, and range from $\lesssim$20 K in DM Tau to a peak of 180 K in HD 100546. A handful of disks show local increases or decreases in gas temperature, some of which correspond to the radial locations of known millimeter dust features or proposed embedded planets.

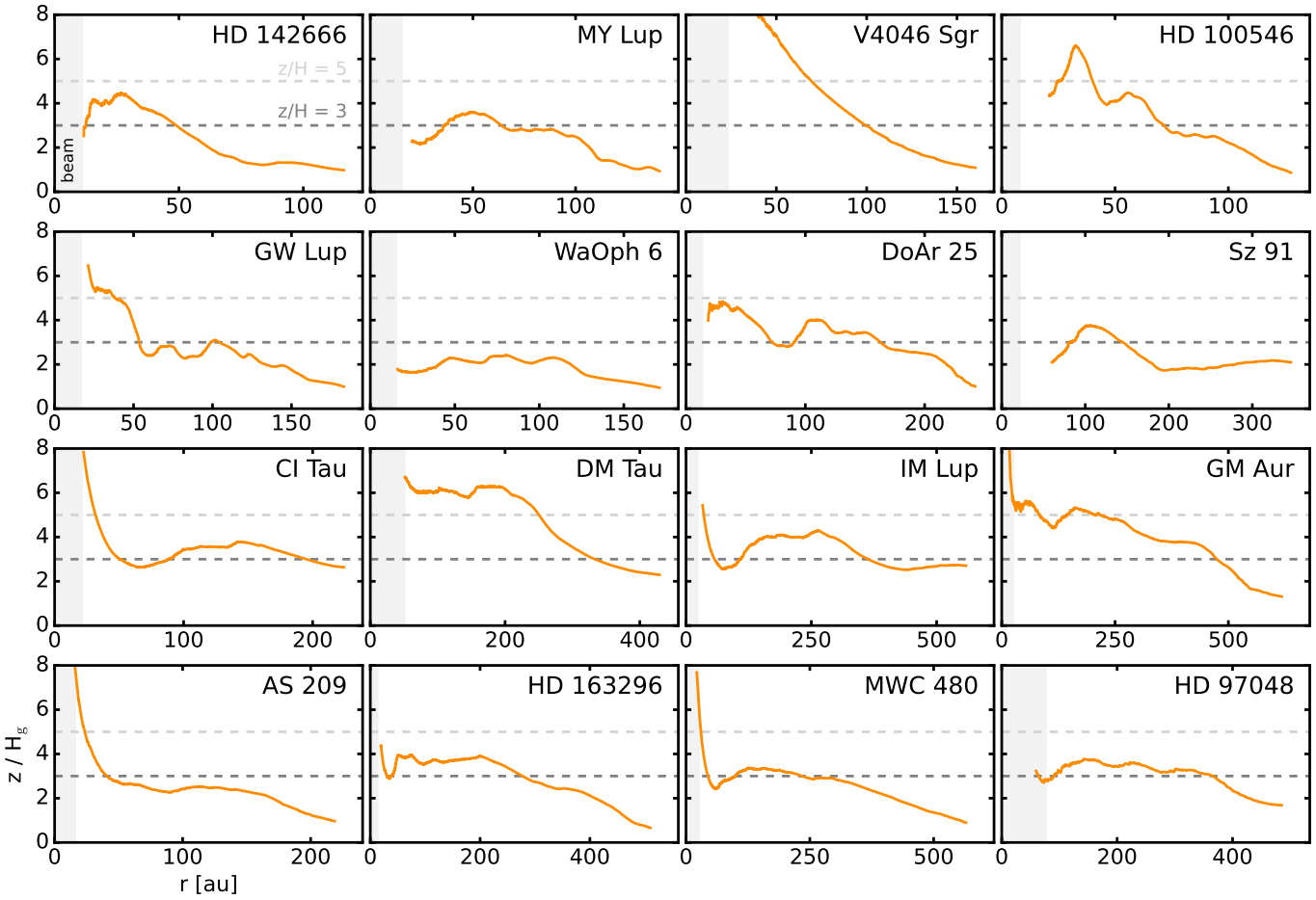

Figure 12. Ratio of CO emission surfaces and gas pressure scale heights for all disks in our sample. Dashed gray lines show constant ratios of three and five. Each disk has a different radial range, corresponding to the range where we were able to extract emission surfaces. The inner gray shaded region is the FWHM of the beam major axis.

5. By combining our sample with literature sources, including the MAPS disks, that have previously mapped CO emission surfaces, we find that emission surface heights weakly decline with stellar host mass and mean gas temperature. Due to the large scatter present, these trends are only suggestive but are generally consistent with expectations from simple scaling relations. We also identify a strong positive correlation between emission surface z/r and CO gas disk size, which is largely due to the flared nature of line emission surfaces in disks.

6. We compare the derived CO emission surfaces to the gas pressure scale heights in our disk sample. We find that, on average, the CO emission surface traces $\approx$2-5$\times$H$_g$. We also identify a tentative trend between CO gas disk size and the ratio of line emission height and scale height, which suggests that CO line emission surfaces could be calibrated as empirical tracers of average H$_g$ values.

7. We also derived dynamical masses and CO gas disk sizes for all disks in our sample. Dynamical masses are consistent with literature estimates, except for WaOph 6 where we find $M_* = 1.12$ M$_\odot$, which is $\approx$1.1-2.0$\times$ larger than previous stellar evolutionary model estimates.

We have shown an effective method for extracting CO emitting layers in a large sample of disks. Such a method can naturally be extended to comparable observations of CO isotopologue lines, which allows a full mapping of 2D disk structure and temperature (e.g., Pinte et al. 2018; Law et al. 2021a), or to other important molecular tracers of disk chemistry and structure (e.g., Teague & Loomis 2020; Bergner et al. 2021). Higher sensitivity CO line emission data are also necessary to better characterize the prevalence and nature of vertical substructures, and how they relate to other disk characteristics.

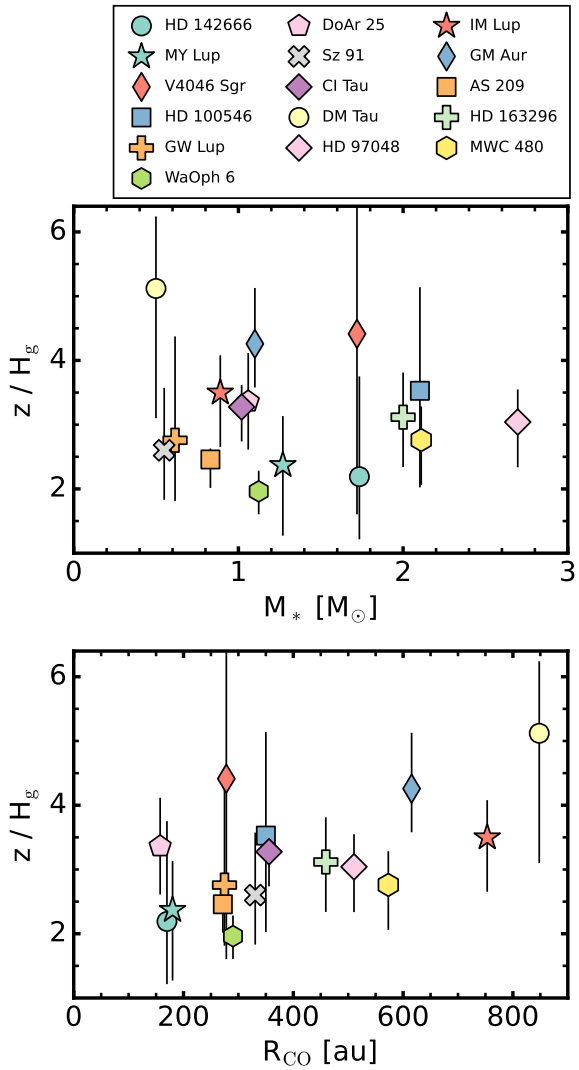

Figure 13. Average $z/H_{\rm g}$ ratios versus stellar mass (top) and CO gas disk size (bottom). Markers show the 50th percentile, while vertical lines show the 16th to 84th percentile range, calculated from the profiles in Figure 12.

This paper makes use of the following ALMA data: ADS/JAO.ALMA#2012.1.00761.S, 2015.1.00192.S, 2016.1.00315.S, 2016.1.00344.S, 2016.1.00484.L, 2016.1.00724.S, and 2017.A.00014.S. ALMA is a partnership of ESO (representing its member states), NSF (USA) and NINS (Japan), together with NRC (Canada), MOST and ASIAA (Taiwan), and KASI (Republic of Korea), in cooperation with the Republic of Chile. The Joint ALMA Observatory is operated by ESO, AUI/NRAO and NAOJ. The National Radio Astronomy Observatory is a facility of the National Science Foundation operated under cooperative agreement by Associated Universities, Inc.

C.J.L. thanks Gerrit van der Plas, Simon Casassus, Linda Podio, and Christian Flores for providing data for HD 97048, HD 135344B, IRAS 04302+2247, and Oph 163131, respectively.

C.J.L. acknowledges funding from the National Science Foundation Graduate Research Fellowship under Grant No. DGE1745303. R.T. and F.L. acknowledge support from the Smithsonian Institution as a Submillimeter Array (SMA) Fellow. K.I.Ö. acknowledges support from the Simons Foundation (SCOL #321183) and an NSF AAG Grant (#1907653). E.A.R acknowledges support from NSF AST 1830728. T.T. is supported by JSPS KAKENHI Grant Numbers JP17K14244 and JP20K04017. S.P. acknowledges support ANID/FONDECYT Regular grant 1191934 and Millennium Nucleus NCN2021080 grant. J.D.I. acknowledges support from the Science and Technology Facilities Council of the United Kingdom (STFC) under ST/T000287/1. S.M.A. and J.H. acknowledge funding support from the National Aeronautics and Space Administration under Grant No. 17-XRP17 2-0012 issued through the Exoplanets Research Program. Support for J.H. was provided by NASA through the NASA Hubble Fellowship grant #HST-HF2-51460.001-A awarded by the Space Telescope Science Institute, which is operated by the Association of Universities for Research in Astronomy, Inc., for NASA, under contract NAS5-26555. G.P.R. acknowledges support from the Netherlands Organisation for Scientific Research (NWO, program number 016.Veni.192.233). L.M.P. gratefully acknowledges support by the ANID BASAL project FB210003, and by ANID, – Millennium Science Initiative Program – NCN19_171. V.V.G. acknowledges support from FONDECYT Iniciación 11180904 and ANID project Basal AFB-170002. J.H.K.'s research is supported by NASA Exoplanets Research Program grant 80NSSC19K0292 to Rochester Institute of Technology. J.B. acknowledges support by NASA through the NASA Hubble Fellowship grant #HST-HF2-51427.001-A awarded by the Space Telescope Science Institute, which is operated by the Association of Universities for Research in Astronomy, Incorporated, under NASA contract NAS5-26555.

Facilities: ALMA

Software: Astropy (Astropy Collaboration et al. 2013; Price-Whelan et al. 2018), `bettermoments` (Teague & Foreman-Mackey 2018), CASA (McMullin et al. 2007), `disksurf` (Teague et al. 2021), `GoFish` (Teague 2019b), `keplerian_mask` (Teague 2020), `linmix` (https://github.com/jmeyers314/linmix), Matplotlib (Hunter 2007), NumPy (van der Walt et al. 2011), SciPy (Virtanen et al. 2020)

APPENDIX

A. CO ZEROTH MOMENT MAPS, RADIAL PROFILES, AND GAS DISK SIZES

All zeroth moment maps shown in Figure 1 were generated using the `bettermoments` (Teague & Foreman-Mackey 2018) python package, closely following the procedures outlined in Law et al. (2021b). Briefly, we adopted Keplerian masks generated using the `keplerian_mask` (Teague 2020) code and based on the stellar+disk parameters listed in Table 1. Each mask was visually inspected to ensure that it contained all emission present in the channel maps and if required, manual adjustments to mask parameters were made, e.g., maximum radius, beam convolution size. For accurate flux recovery, we did not use a flux threshold for pixel inclusion, i.e., sigma clipping. Channels containing either no emission or significant absorption due to cloud contamination were excluded.

Radial intensity profiles were generated using the `radial_profile` function in the `GoFish` python package (Teague 2019b) to deproject the zeroth moment maps. For line emission originating from elevated disk layers like CO, we must consider its emitting surface during the deprojection process. Following Law et al. (2021b), we deprojected radial profiles using the derived surfaces listed in Table 2 for all disks. Radial profiles were generated using azimuthal averages, except for those disks showing substantial cloud obscuration, where we used asymmetric wedges to avoid regions of cloud contamination. This was necessary for WaOph 6 and Sz 91, where we used $\pm55°$ and $\pm90°$ wedges in the southern and northern parts of the disks, respectively. We also used a $\pm30°$ wedge in DoAr 25 along the disk major axis, due to its highly inclined nature, to avoid including the shadowed disk midplane. Figure 14 shows the resultant radial profiles. For further discussion of the zeroth moment map and radial intensity profile generation process, see Sections 2.2 and 2.3, respectively, in Law et al. (2021b).

To measure the radial extent of CO line emission, we calculated the disk size (R_{CO}) as the radius which encloses 90% of the total flux (e.g., Tripathi et al. 2017; Ansdell et al. 2018). This definition also allows for a direct comparison with the size of the MAPS disks derived in the same way in Law et al. (2021b). However, R_{CO} does not always reflect the outermost portion of CO emission in a disk, especially for those sources with low-intensity, plateau-like emission at large radii, e.g., CI Tau, DM Tau. Instead, to measure the outermost edge (R_{edge}) of the CO gas disk, we computed the radius which encloses 99% of the total disk flux. Both measurements were performed using the radial profiles in Figure 14. Table 5 shows the CO gas disk size measurements and both R_{CO} (gray) and R_{edge} (red) are marked in Figure 14. Overall, we find R_{CO} values that are generally consistent with those reported in Long et al. (2022). We do, however, find considerably smaller R_{CO} values for the V4046 Sgr ($\gtrsim$20%) and DoAr 25 ($\gtrsim$30%) disks. For the V4046 Sgr disk, this is likely driven by the coarse angular resolution ($\gtrsim1''$) of the CO observations used by Long et al. (2022), while for the DoAr 25 disk, the ability to draw a wedge precisely along the CO emission

Table 5. Gas Disk Sizes

Source	Line CO	R_{CO} [au]	R_{edge} [au]
HD 142666	J=2−1	170 ± 4	209 ± 15
MY Lup	J=2−1	180 ± 5	231 ± 14
V4046 Sgr	J=3−2	278 ± 7	360 ± 7
HD 100546	J=2−1	350 ± 3	480 ± 4
GW Lup	J=2−1	275 ± 27	424 ± 36
WaOph 6	J=2−1	290 ± 6	435 ± 24
DoAr 25	J=2−1	157 ± 4	214 ± 12
Sz 91	J=3−2	331 ± 6	418 ± 12
CI Tau	J=3−2	356 ± 7	571 ± 19
DM Tau	J=2−1	848 ± 14	1055 ± 23
HD 97048[a]	J=2−1	511 ± 21	733 ± 26
HD 169142[b]	J=2−1	344 ± 6	424 ± 18
HD 135344B[c]	J=2−1	180 ± 31	235 ± 34

[a] Fit using the radial profile derived from reimaged CO J=2–1 data (see Appendix C).

[b] Fit using azimuthally-averaged radial profile from Yu et al. (2021).

[c] Fit using the azimuthally-averaged radial profile generated from the *uv*-tapered, single Gaussian fit map from Casassus et al. (2021).

NOTE—Disk size (R_{CO}) and outer edge (R_{edge}) were computed as the radius which encloses 90% and 99% of the total disk flux, respectively.

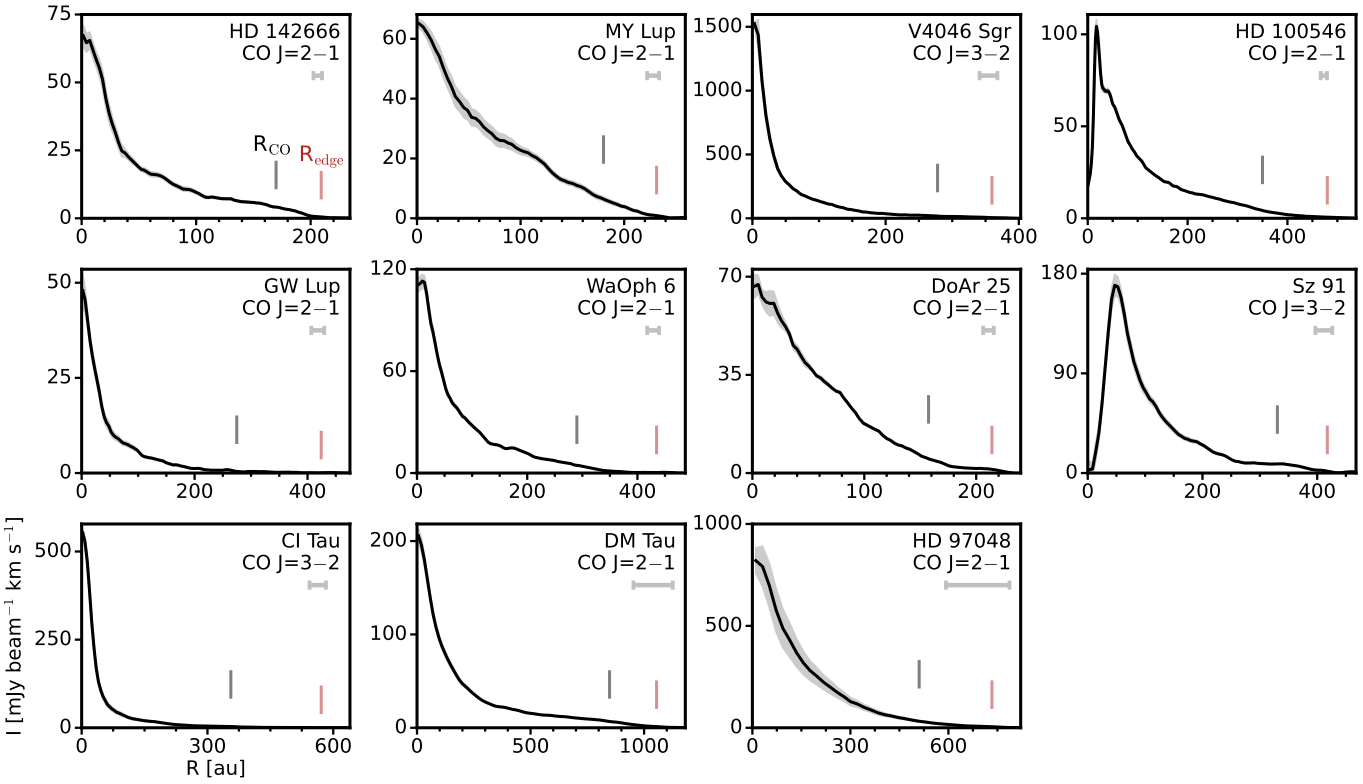

Figure 14. Deprojected radial intensity profiles of CO lines for our sample and the HD 97048 disk. Gray shaded regions show the 1σ uncertainty, measured as the standard error on the mean in the annulus or arc over which the emission was averaged. The radial locations of R_{CO} and R_{edge} from Table 5 are labeled in gray and red, respectively. The FWHM of the major axis of the synthesized beam is shown by a horizontal bar in the upper right corner of each panel.

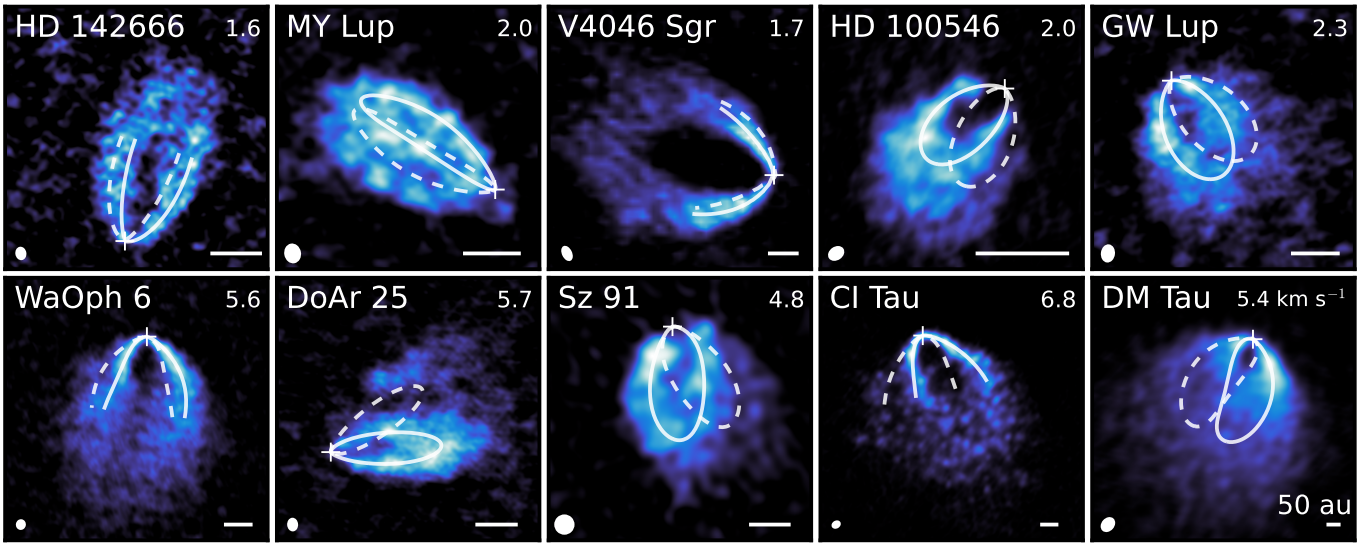

Figure 15. Representative CO line emission channels for each of the disks in our sample. The CO isovelocity contours are derived using the parametric fits in Table 2 and source parameters from Table 4. The extent of the contours corresponds to only those radial regions where we have direct constraints on the line emission surface. Crosses mark the centers of each disk. Solid curves indicate the upper surface of the disk and dashed curves mark the lower surface. Kinematic Local Standard of Rest (LSRK) velocities are marked in the upper right corner. The synthesized beam and a scale bar indicating 50 au is shown in the lower left and right corner, respectively, of each panel.

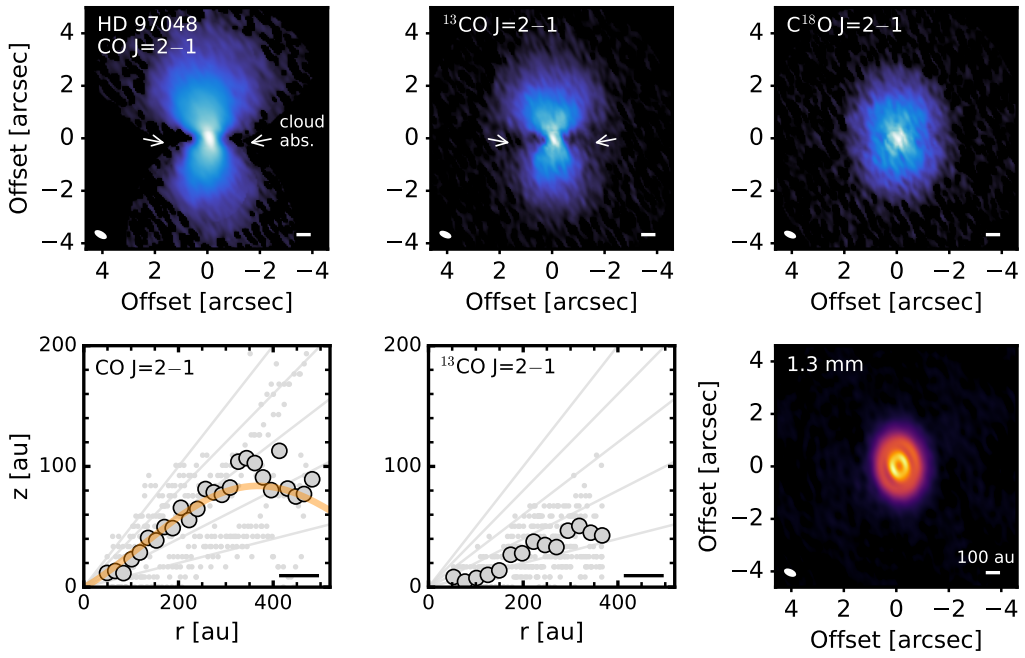

Figure 16. From left to right, top to bottom: CO, ^{13}CO, and C^{18}O J=2–1 zeroth moment maps; CO and ^{13}CO line emission surfaces; and 1.3 mm continuum image. The synthesized beam and a scale bar indicating 100 au is shown in the lower left and right corner, respectively, of each image. Regions of cloud contamination in the CO and ^{13}CO J=2–1 lines are marked with arrows. Large gray points show radially-binned surfaces and small, light gray points represent individual measurements. The orange line in the CO emission surface show the exponentially-tapered power law fit (Table 2).

surface to avoid confusion from the disk midplane likely leads to an improved estimate of R_{CO}.

B. ISOVELOCITY CONTOURS

Figure 15 shows the predicted isovelocity contours for CO line emission in representative channels in our sample. We show contours for only those radii where we were able to directly constrain the CO line emitting heights.

C. IMAGING AND RE-ANALYSIS OF HD 97048 ALMA DATA

The CO J=2–1 emission surface of HD 97048 (CU Cha) was extracted by Rich et al. (2021) using archival ALMA data (PI: G. van der Plas, 2015.1.00192.S)[5]. However, the archival data does not provide continuum+line image cubes necessary for extracting temperatures (Section 3.4.1).

We re-imaged both the line-only and line+continuum CO data for this disk. Since the line-only data was taken from the pipeline-produced images, we also reprocessed this data to improve image quality. Since this ALMA program contained ^{13}CO and C^{18}O J=2–1 isotopologue data, we also processed and imaged these line data. In CASA `v4.7.2` (McMullin et al. 2007), the 1.3 mm continuum was self-calibrated using two rounds of phase self-calibration, which was then applied to the continuum-subtracted line data. Both continuum and line imaging was performed with `tclean` with uniform weighting, which resulted in the 1.3 mm continuum image having a beam size of 0.″43 × 0.″21, PA=23.8° and an rms of 0.08 mJy/beam. The CO J=2–1 data had a beam size of 0.″45 × 0.″20 with PA=30°, while the ^{13}CO J=2–1 and C^{18}O J=2–1 data had beam sizes of 0.″42 × 0.″18 with PA=23°. Typical line rms values were ≈5-9 mJy/beam. Figure 16 shows the 1.3 mm continuum image and the zeroth moment maps for CO, ^{13}CO, and C^{18}O J=2–1 produced with `bettermoments` as in Appendix A.

As in Section 2.2, we used `disksurf` to extract emission surfaces for the CO J=2–1 and ^{13}CO J=2–1 lines but were unable to derive line emitting heights for C^{18}O J=2–1. We find a CO emission surface that is consistent with the one derived in Rich et al. (2021). Due to the coarse and elongated beam size, it is possible that the CO and ^{13}CO J=2–1 emission surfaces are modestly underestimated. However, we note that Pinte et al. (2019) found a ^{13}CO J=3–2 emission height of 17 au at a radius of 130 au using a ≈0.″1 beam and similar surface extraction method. This closely agrees with the ^{13}CO J=2–1 height that we derived at the same radius.

[5] We note that the ALMA project code 2016.1.00826.S is incorrectly cited in Rich et al. (2021), but the authors instead used the CO J=2–1 transition from 2015.1.00192.S.

Table 6. Characteristic z/r of CO Emission Surfaces

Source	Line	$r_{\rm cutoff}$ [au]	z/r
This work:			
HD 142666[a]	J=2−1	51	$0.20^{+0.02}_{-0.05}$
MY Lup	J=2−1	101	$0.16^{+0.01}_{-0.06}$
V4046 Sgr	J=3−2	114	$0.24^{+0.12}_{-0.07}$
HD 100546	J=2−1	88	$0.24^{+0.07}_{-0.05}$
GW Lup	J=2−1	150	$0.21^{+0.13}_{-0.02}$
WaOph 6	J=2−1	110	$0.19^{+0.03}_{-0.05}$
DoAr 25	J=2−1	177	$0.25^{+0.04}_{-0.06}$
Sz 91[b]	J=3−2	108	$0.22^{+0.05}_{-0.10}$
CI Tau	J=3−2	224	$0.24^{+0.07}_{-0.04}$
DM Tau	J=2−1	204	$0.53^{+0.04}_{-0.09}$
Literature:			
IM Lup[a]	J=2−1	300	$0.34^{+0.08}_{-0.11}$
GM Aur	J=2−1	479	$0.35^{+0.06}_{-0.11}$
AS 209	J=2−1	173	$0.17^{+0.04}_{-0.07}$
HD 163296	J=2−1	191	$0.24^{+0.06}_{-0.09}$
MWC 480	J=2−1	401	$0.22^{+0.05}_{-0.11}$
HD 97048	J=2−1	403	$0.26^{+0.05}_{-0.03}$

[a]Cutoff radius manually adjusted.

[b]Emission surface data were averaged starting at >50 au.

NOTE—Literature sample composed of the disks around IM Lup, GM Aur, AS 209, HD 163296, and MWC 480 (Law et al. 2021a); and HD 97048 (Rich et al. 2021) with directly mapped CO line emission surfaces. Characteristic z/r values are computed as the 50th percentile interior to $r_{\rm cutoff}$ and the uncertainties show the 16th to 84th percentile range.

Radial and 2D temperature profiles were calculated using the line+continuum cubes, as in Section 3.4, and are shown in Figures 6 and 7.

D. DEFINITION OF CHARACTERISTIC Z/R OF CO EMISSION SURFACES

To enable a homogeneous comparison among sources, we required a characteristic z/r for each CO line emission surface. We chose this z/r to describe the inner rising portions of the line emission surfaces before the surfaces being to plateau and turnover due to, e.g., decreasing gas surface densities or insufficient observational line sensitivities. We defined this quantity as the mean z/r computed from all points in the binned surfaces interior to a fixed cutoff radius. We chose $r_{\rm cutoff} = 0.8 \times r_{\rm taper}$, where $r_{\rm taper}$ is the fitted parameter from the exponentially-tapered power laws from Table 2. We visually confirmed that 80% of $r_{\rm taper}$ only included the rising part of the emission surfaces for all sources in our sample and in literature sources with directly mapped line emitting heights (Law et al. 2021a; Rich et al. 2021) with the exception of HD 142666 and IM Lup. For these two disks, $r_{\rm cutoff}$ was manually chosen due to the lack of a clear turnover phase in either of their emission surfaces. Due to the relatively flat inner portion of the emission surface of the Sz 91 disk, we only averaged those points beyond 50 au when computing its characteristic z/r. We also calculated the 16th to 84th percentile range within $r_{\rm cutoff}$ as a proxy of the lower and upper flaring ranges, respectively, for each surface. Table 6 lists the characteristic z/r, flaring ranges, and $r_{\rm cutoff}$ values for all sources in our sample and from the literature.

The characteristic z/r is, by definition, constant and generally matches the binned surfaces well. However, at large radii, near $r_{\rm cutoff}$, this z/r sometimes modestly underestimates the measured CO emission surface. This is the result of the flared nature of line emission surfaces and can be clearly in several sources, e.g., CI Tau, Sz 91, IM Lup, HD 163296, in Figure 17.

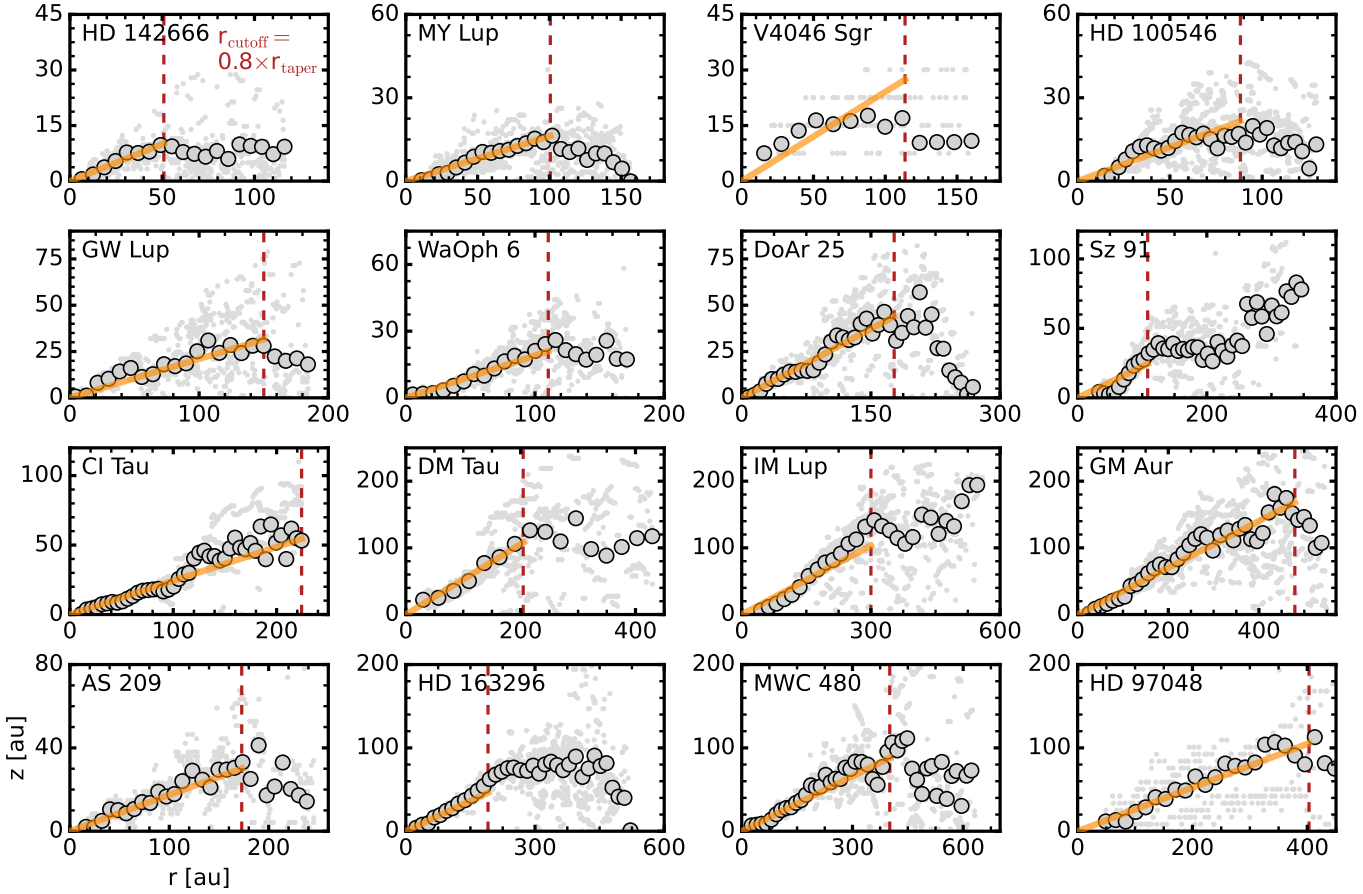

Figure 17. Gallery for CO line emission surfaces for our sample and the IM Lup, GM Aur, AS 209, HD 163296, MWC 480 (Law et al. 2021a) and HD 97048 disks (Rich et al. 2021). Large gray points show radially-binned surfaces and small, light gray points represent individual measurements. Characteristic z/r values are shown in orange and were computed as the mean z/r for radii within $r_{cutoff} = 0.8 \times r_{taper}$, which is marked by a dashed red line.

REFERENCES

Alarcón, F., Bosman, A. D., Bergin, E. A., et al. 2021, ApJS, 257, 8, doi: 10.3847/1538-4365/ac22ae

Andrews, S. M., Wilner, D. J., Espaillat, C., et al. 2011, ApJ, 732, 42, doi: 10.1088/0004-637X/732/1/42

Andrews, S. M., Huang, J., Pérez, L. M., et al. 2018, ApJL, 869, L41, doi: 10.3847/2041-8213/aaf741

Ansdell, M., Williams, J. P., Trapman, L., et al. 2018, ApJ, 859, 21, doi: 10.3847/1538-4357/aab890

Asensio-Torres, R., Henning, T., Cantalloube, F., et al. 2021, A&A, 652, A101, doi: 10.1051/0004-6361/202140325

Astropy Collaboration, Robitaille, T. P., Tollerud, E. J., et al. 2013, A&A, 558, A33, doi: 10.1051/0004-6361/201322068

Avenhaus, H., Quanz, S. P., Meyer, M. R., et al. 2014, ApJ, 790, 56, doi: 10.1088/0004-637X/790/1/56

Avenhaus, H., Quanz, S. P., Garufi, A., et al. 2018, ApJ, 863, 44, doi: 10.3847/1538-4357/aab846

Bae, J., Teague, R., & Zhu, Z. 2021, ApJ, 912, 56, doi: 10.3847/1538-4357/abe45e

Bailer-Jones, C. A. L., Rybizki, J., Fouesneau, M., Demleitner, M., & Andrae, R. 2021, AJ, 161, 147, doi: 10.3847/1538-3881/abd806

Benisty, M., Tatulli, E., Ménard, F., & Swain, M. R. 2010, A&A, 511, A75, doi: 10.1051/0004-6361/200913590

Bergner, J. B., Öberg, K. I., Guzmán, V. V., et al. 2021, ApJS, 257, 11, doi: 10.3847/1538-4365/ac143a

Berné, O., Fuente, A., Pantin, E., et al. 2015, A&A, 578, L8, doi: 10.1051/0004-6361/201526041

Binks, A. S., & Jeffries, R. D. 2014, MNRAS, 438, L11, doi: 10.1093/mnrasl/slt141

Boehler, Y., Weaver, E., Isella, A., et al. 2017, ApJ, 840, 60, doi: 10.3847/1538-4357/aa696c

Brown-Sevilla, S. B., Keppler, M., Barraza-Alfaro, M., et al. 2021, A&A, 654, A35, doi: 10.1051/0004-6361/202140783

Bruderer, S., van Dishoeck, E. F., Doty, S. D., & Herczeg, G. J. 2012, A&A, 541, A91, doi: 10.1051/0004-6361/201118218

Calahan, J. K., Bergin, E. A., Zhang, K., et al. 2021, ApJS, 257, 17, doi: 10.3847/1538-4365/ac143f

Calcino, J., Hilder, T., Price, D. J., et al. 2022, ApJL, 929, L25, doi: 10.3847/2041-8213/ac64a7

Canovas, H., Caceres, C., Schreiber, M. R., et al. 2016, MNRAS, 458, L29, doi: 10.1093/mnrasl/slw006

Canovas, H., Schreiber, M. R., Cáceres, C., et al. 2015, ApJ, 805, 21, doi: 10.1088/0004-637X/805/1/21

Casassus, S., & Pérez, S. 2019, ApJL, 883, L41, doi: 10.3847/2041-8213/ab4425

Casassus, S., Christiaens, V., Cárcamo, M., et al. 2021, MNRAS, 507, 3789, doi: 10.1093/mnras/stab2359

Chiang, E. I., & Goldreich, P. 1997, ApJ, 490, 368, doi: 10.1086/304869

Clarke, C. J., Tazzari, M., Juhasz, A., et al. 2018, ApJL, 866, L6, doi: 10.3847/2041-8213/aae36b

Cleeves, L. I. 2016, ApJL, 816, L21, doi: 10.3847/2041-8205/816/2/L21

D'Alessio, P., Cantö, J., Calvet, N., & Lizano, S. 1998, ApJ, 500, 411, doi: 10.1086/305702

Dartois, E., Dutrey, A., & Guilloteau, S. 2003, A&A, 399, 773, doi: 10.1051/0004-6361:20021638

de Gregorio-Monsalvo, I., Ménard, F., Dent, W., et al. 2013, A&A, 557, A133, doi: 10.1051/0004-6361/201321603

Disk Dynamics Collaboration, Armitage, P. J., Bae, J., et al. 2020, arXiv e-prints, arXiv:2009.04345. https://arxiv.org/abs/2009.04345

Donati, J. F., Bouvier, J., Alencar, S. H., et al. 2020, MNRAS, 491, 5660, doi: 10.1093/mnras/stz3368

Dong, R., Liu, S.-Y., & Fung, J. 2019, ApJ, 870, 72, doi: 10.3847/1538-4357/aaf38e

D'Orazi, V., Gratton, R., Desidera, S., et al. 2019, Nature Astronomy, 3, 167, doi: 10.1038/s41550-018-0626-6

Dullemond, C. P., Dominik, C., & Natta, A. 2001, ApJ, 560, 957, doi: 10.1086/323057

Dullemond, C. P., Birnstiel, T., Huang, J., et al. 2018, ApJL, 869, L46, doi: 10.3847/2041-8213/aaf742

Dutrey, A., Guilloteau, S., Piétu, V., et al. 2017, A&A, 607, A130, doi: 10.1051/0004-6361/201730645

Facchini, S., Birnstiel, T., Bruderer, S., & van Dishoeck, E. F. 2017, A&A, 605, A16, doi: 10.1051/0004-6361/201630329

Facchini, S., Pinilla, P., van Dishoeck, E. F., & de Juan Ovelar, M. 2018, A&A, 612, A104, doi: 10.1051/0004-6361/201731390

Fedele, D., Toci, C., Maud, L., & Lodato, G. 2021, A&A, 651, A90, doi: 10.1051/0004-6361/202141278

Fedele, D., van Dishoeck, E. F., Kama, M., Bruderer, S., & Hogerheijde, M. R. 2016, A&A, 591, A95, doi: 10.1051/0004-6361/201526948

Fedele, D., Carney, M., Hogerheijde, M. R., et al. 2017, A&A, 600, A72, doi: 10.1051/0004-6361/201629860

Flaherty, K., Hughes, A. M., Simon, J. B., et al. 2020, ApJ, 895, 109, doi: 10.3847/1538-4357/ab8cc5

Flores, C., Duchêne, G., Wolff, S., et al. 2021, AJ, 161, 239, doi: 10.3847/1538-3881/abeb1e

Fogel, J. K. J., Bethell, T. J., Bergin, E. A., Calvet, N., & Semenov, D. 2011, ApJ, 726, 29, doi: 10.1088/0004-637X/726/1/29

Foreman-Mackey, D., Hogg, D. W., Lang, D., & Goodman, J. 2013, PASP, 125, 306, doi: 10.1086/670067

Gaia Collaboration, Brown, A. G. A., Vallenari, A., et al. 2021, A&A, 649, A1, doi: 10.1051/0004-6361/202039657

Garufi, A., Quanz, S. P., Schmid, H. M., et al. 2016, A&A, 588, A8, doi: 10.1051/0004-6361/201527940

Garufi, A., Avenhaus, H., Pérez, S., et al. 2020, A&A, 633, A82, doi: 10.1051/0004-6361/201936946

Garufi, A., Podio, L., Codella, C., et al. 2021, A&A, 645, A145, doi: 10.1051/0004-6361/202039483

Garufi, A., Dominik, C., Ginski, C., et al. 2022, A&A, 658, A137, doi: 10.1051/0004-6361/202141692

Ginski, C., Stolker, T., Pinilla, P., et al. 2016, A&A, 595, A112, doi: 10.1051/0004-6361/201629265

Guilloteau, S., Simon, M., Piétu, V., et al. 2014, A&A, 567, A117, doi: 10.1051/0004-6361/201423765

Guilloteau, S., Piétu, V., Chapillon, E., et al. 2016, A&A, 586, L1, doi: 10.1051/0004-6361/201527620

Haworth, T. J., Facchini, S., Clarke, C. J., & Cleeves, L. I. 2017, MNRAS, 468, L108, doi: 10.1093/mnrasl/slx037

Huang, J., Andrews, S. M., Dullemond, C. P., et al. 2018, ApJL, 869, L42, doi: 10.3847/2041-8213/aaf740

Hunter, J. D. 2007, Computing in Science and Engineering, 9, 90, doi: 10.1109/MCSE.2007.55

Ilee, J. D., Walsh, C., Booth, A. S., et al. 2021, ApJS, 257, 9, doi: 10.3847/1538-4365/ac1441

Ilgner, M., Henning, T., Markwick, A. J., & Millar, T. J. 2004, A&A, 415, 643, doi: 10.1051/0004-6361:20034061

Isella, A., Huang, J., Andrews, S. M., et al. 2018, ApJL, 869, L49, doi: 10.3847/2041-8213/aaf747

Izquierdo, A. F., Facchini, S., Rosotti, G. P., van Dishoeck, E. F., & Testi, L. 2022, ApJ, 928, 2, doi: 10.3847/1538-4357/ac474d

Kelly, B. C. 2007, ApJ, 665, 1489, doi: 10.1086/519947

Kenyon, S. J., & Hartmann, L. 1987, ApJ, 323, 714, doi: 10.1086/165866

Kudo, T., Hashimoto, J., Muto, T., et al. 2018, ApJL, 868, L5, doi: 10.3847/2041-8213/aaeb1c

Law, C. J., Teague, R., Loomis, R. A., et al. 2021a, ApJS, 257, 4, doi: 10.3847/1538-4365/ac1439

Law, C. J., Loomis, R. A., Teague, R., et al. 2021b, ApJS, 257, 3, doi: 10.3847/1538-4365/ac1434

Long, F., Pinilla, P., Herczeg, G. J., et al. 2018, ApJ, 869, 17, doi: 10.3847/1538-4357/aae8e1

Long, F., Andrews, S. M., Vega, J., et al. 2021, ApJ, 915, 131, doi: 10.3847/1538-4357/abff53

Long, F., Andrews, S. M., Rosotti, G., et al. 2022, arXiv e-prints, arXiv:2203.16735. https://arxiv.org/abs/2203.16735

Mamajek, E. E., & Bell, C. P. M. 2014, MNRAS, 445, 2169, doi: 10.1093/mnras/stu1894

Maucó, K., Olofsson, J., Canovas, H., et al. 2020, MNRAS, 492, 1531, doi: 10.1093/mnras/stz3380

McMullin, J. P., Waters, B., Schiebel, D., Young, W., & Golap, K. 2007, in Astronomical Society of the Pacific Conference Series, Vol. 376, Astronomical Data Analysis Software and Systems XVI, ed. R. A. Shaw, F. Hill, & D. J. Bell, 127

Monnier, J. D., Harries, T. J., Aarnio, A., et al. 2017, ApJ, 838, 20, doi: 10.3847/1538-4357/aa6248

Morbidelli, A., Szulágyi, J., Crida, A., et al. 2014, Icarus, 232, 266, doi: 10.1016/j.icarus.2014.01.010

Muro-Arena, G. A., Dominik, C., Waters, L. B. F. M., et al. 2018, A&A, 614, A24, doi: 10.1051/0004-6361/201732299

Öberg, K. I., Cleeves, L. I., Bergner, J. B., et al. 2021a, AJ, 161, 38, doi: 10.3847/1538-3881/abc74d

Öberg, K. I., Guzmán, V. V., Walsh, C., et al. 2021b, ApJS, 257, 1, doi: 10.3847/1538-4365/ac1432

Paneque-Carreño, T., Pérez, L. M., Benisty, M., et al. 2021, ApJ, 914, 88, doi: 10.3847/1538-4357/abf243

Pegues, J., Czekala, I., Andrews, S. M., et al. 2021, ApJ, 908, 42, doi: 10.3847/1538-4357/abd4eb

Pérez, S., Casassus, S., & Benítez-Llambay, P. 2018, MNRAS, 480, L12, doi: 10.1093/mnrasl/sly109

Perez, S., Dunhill, A., Casassus, S., et al. 2015, ApJL, 811, L5, doi: 10.1088/2041-8205/811/1/L5

Pérez, S., Casassus, S., Hales, A., et al. 2020, ApJL, 889, L24, doi: 10.3847/2041-8213/ab6b2b

Piétu, V., Dutrey, A., & Guilloteau, S. 2007, A&A, 467, 163, doi: 10.1051/0004-6361:20066537

Pineda, J. E., Quanz, S. P., Meru, F., et al. 2014, ApJL, 788, L34, doi: 10.1088/2041-8205/788/2/L34

Pineda, J. E., Szulágyi, J., Quanz, S. P., et al. 2019, ApJ, 871, 48, doi: 10.3847/1538-4357/aaf389

Pinte, C., Ménard, F., Duchêne, G., et al. 2018, A&A, 609, A47, doi: 10.1051/0004-6361/201731377

Pinte, C., van der Plas, G., Ménard, F., et al. 2019, Nature Astronomy, 3, 1109, doi: 10.1038/s41550-019-0852-6

Pinte, C., Price, D. J., Ménard, F., et al. 2020, ApJL, 890, L9, doi: 10.3847/2041-8213/ab6dda

Podio, L., Garufi, A., Codella, C., et al. 2020, A&A, 642, L7, doi: 10.1051/0004-6361/202038952

Price-Whelan, A. M., Sipőcz, B. M., Günther, H. M., et al. 2018, AJ, 156, 123, doi: 10.3847/1538-3881/aabc4f

Pyerin, M. A., Delage, T. N., Kurtovic, N. T., et al. 2021, A&A, 656, A150, doi: 10.1051/0004-6361/202141998

Quast, G. R., Torres, C. A. O., de La Reza, R., da Silva, L., & Mayor, M. 2000, IAU Symposium, 200, 28

Rab, C., Kamp, I., Dominik, C., et al. 2020, A&A, 642, A165, doi: 10.1051/0004-6361/202038712

Rich, E. A., Wisniewski, J. P., Sitko, M. L., et al. 2020, ApJ, 902, 4, doi: 10.3847/1538-4357/abb2a3

Rich, E. A., Teague, R., Monnier, J. D., et al. 2021, ApJ, 913, 138, doi: 10.3847/1538-4357/abf92e

Romero, G. A., Schreiber, M. R., Cieza, L. A., et al. 2012, ApJ, 749, 79, doi: 10.1088/0004-637X/749/1/79

Rosenfeld, K. A., Andrews, S. M., Hughes, A. M., Wilner, D. J., & Qi, C. 2013, ApJ, 774, 16, doi: 10.1088/0004-637X/774/1/16

Rosenfeld, K. A., Andrews, S. M., Wilner, D. J., & Stempels, H. C. 2012, ApJ, 759, 119, doi: 10.1088/0004-637X/759/2/119

Rosotti, G. P., Ilee, J. D., Facchini, S., et al. 2021, MNRAS, 501, 3427, doi: 10.1093/mnras/staa3869

Ruíz-Rodríguez, D., Kastner, J., Hily-Blant, P., & Forveille, T. 2021, A&A, 646, A59, doi: 10.1051/0004-6361/202038209

Ruíz-Rodríguez, D., Kastner, J. H., Dong, R., et al. 2019, AJ, 157, 237, doi: 10.3847/1538-3881/ab1c58

Schwarz, K. R., Calahan, J. K., Zhang, K., et al. 2021, ApJS, 257, 20, doi: 10.3847/1538-4365/ac143b

Semenov, D., & Wiebe, D. 2011, ApJS, 196, 25, doi: 10.1088/0067-0049/196/2/25

Simon, M., Guilloteau, S., Di Folco, E., et al. 2017, ApJ, 844, 158, doi: 10.3847/1538-4357/aa78f1

Simon, M., Guilloteau, S., Beck, T. L., et al. 2019, ApJ, 884, 42, doi: 10.3847/1538-4357/ab3e3b

Sissa, E., Gratton, R., Garufi, A., et al. 2018, A&A, 619, A160, doi: 10.1051/0004-6361/201732332

Teague, R. 2019a, The Journal of Open Source Software, 4, 1220, doi: 10.21105/joss.01220

—. 2019b, The Journal of Open Source Software, 4, 1632, doi: 10.21105/joss.01632

Teague, R. 2020, richteague/keplerian_mask: Initial Release, 1.0, Zenodo, doi: 10.5281/zenodo.4321137

Teague, R., Bae, J., & Bergin, E. A. 2019, Nature, 574, 378, doi: 10.1038/s41586-019-1642-0

Teague, R., Bae, J., Birnstiel, T., & Bergin, E. A. 2018, ApJ, 868, 113, doi: 10.3847/1538-4357/aae836

Teague, R., & Foreman-Mackey, D. 2018, Bettermoments: A Robust Method To Measure Line Centroids, v1.0, Zenodo, doi: 10.5281/zenodo.1419754

Teague, R., Jankovic, M. R., Haworth, T. J., Qi, C., & Ilee, J. D. 2020, MNRAS, 495, 451, doi: 10.1093/mnras/staa1167

Teague, R., Law, C. J., Huang, J., & Meng, F. 2021, Journal of Open Source Software, 6, 3827, doi: 10.21105/joss.03827

Teague, R., & Loomis, R. 2020, ApJ, 899, 157, doi: 10.3847/1538-4357/aba956

Teague, R., Bae, J., Aikawa, Y., et al. 2021, ApJS, 257, 18, doi: 10.3847/1538-4365/ac1438

Torres, C. A. O., Quast, G. R., da Silva, L., et al. 2006, A&A, 460, 695, doi: 10.1051/0004-6361:20065602

Tripathi, A., Andrews, S. M., Birnstiel, T., & Wilner, D. J. 2017, ApJ, 845, 44, doi: 10.3847/1538-4357/aa7c62

Tsukagoshi, T., Momose, M., Kitamura, Y., et al. 2019, ApJ, 871, 5, doi: 10.3847/1538-4357/aaf4f1

van den Ancker, M. E., de Winter, D., & Tjin A Djie, H. R. E. 1998, A&A, 330, 145

van der Marel, N., Williams, J. P., & Bruderer, S. 2018, ApJL, 867, L14, doi: 10.3847/2041-8213/aae88e

van der Plas, G., Wright, C. M., Ménard, F., et al. 2017, A&A, 597, A32, doi: 10.1051/0004-6361/201629523

van der Walt, S., Colbert, S. C., & Varoquaux, G. 2011, Computing in Science and Engineering, 13, 22, doi: 10.1109/MCSE.2011.37

Veronesi, B., Paneque-Carreño, T., Lodato, G., et al. 2021, ApJL, 914, L27, doi: 10.3847/2041-8213/abfe6a

Villenave, M., Ménard, F., Dent, W. R. F., et al. 2020, A&A, 642, A164, doi: 10.1051/0004-6361/202038087

Villenave, M., Stapelfeldt, K. R., Duchene, G., et al. 2022, arXiv e-prints, arXiv:2204.00640. https://arxiv.org/abs/2204.00640

Vioque, M., Oudmaijer, R. D., Baines, D., Mendigutía, I., & Pérez-Martínez, R. 2018, A&A, 620, A128, doi: 10.1051/0004-6361/201832870

Virtanen, P., Gommers, R., Oliphant, T. E., et al. 2020, Nature Methods, doi: https://doi.org/10.1038/s41592-019-0686-2

Walsh, C., Juhász, A., Meeus, G., et al. 2016, ApJ, 831, 200, doi: 10.3847/0004-637X/831/2/200

Walsh, C., Millar, T. J., & Nomura, H. 2010, ApJ, 722, 1607, doi: 10.1088/0004-637X/722/2/1607

Walsh, C., Juhász, A., Pinilla, P., et al. 2014, ApJL, 791, L6, doi: 10.1088/2041-8205/791/1/L6

Weaver, E., Isella, A., & Boehler, Y. 2018, ApJ, 853, 113, doi: 10.3847/1538-4357/aaa481

Williams, J. P., & Cieza, L. A. 2011, ARA&A, 49, 67, doi: 10.1146/annurev-astro-081710-102548

Yu, H., Teague, R., Bae, J., & Öberg, K. 2021, ApJL, 920, L33, doi: 10.3847/2041-8213/ac283e

Zhang, K., Booth, A. S., Law, C. J., et al. 2021, ApJS, 257, 5, doi: 10.3847/1538-4365/ac1580